AN ABSTRACT OF THE THESIS OF

Justin Lee Elser for the degree of Doctor of Philosophy in Physics presented on September 25, 2008.

Title: Electromagnetic Properties of Anisotropic Plasmonic Metamaterials

Abstract approved: _____

Viktor A. Podolskiy

In this dissertation we study the electromagnetic properties of plasmonic metamaterials. We develop an analytical description to solve the fundamental problem of free-space scattering in planar plasmonic systems by utilizing anisotropic metamaterials. We show with exact numerical simulations that these manufactured materials do completely eliminate the scattering, and even in the case of fabrication defects the scattering is greatly minimized.

We further show that the standard effective medium theory calculations for the cases of anisotropic metamaterials constructed of metal-dielectric layers fails to account for nonlocal effects in the cases where the constituent materials have large differences in permittivity. We show how it is possible to construct a plasmon waveguide out of such a structure and describe a new naming scheme based on the bulk plasmon modes that are supported.

Finally, we study the effective medium theory applied to the case of plasmonic wires embedded in a dielectric host. We describe the effect the geometric properties of the structure has on effective permittivities. For example, we show that a 10% stretching/compression of the distance between nanowires can change the sign of elements of the permittivity tensor.

These results can be applied to high-performance optical sensing, optical polarizers, novel lenses including the hyper- and superlenses, and subdiffraction imaging.

Electromagnetic Properties of Anisotropic Plasmonic Metamaterials

by

Justin Lee Elser

A THESIS

submitted to

Oregon State University

in partial fulfillment of
the requirements for the
degree of

Doctor of Philosophy

Presented September 25, 2008
Commencement June 2009

Doctor of Philosophy thesis of Justin Lee Elser presented on September 25, 2008

APPROVED:

Major Professor, representing Physics

Chair of the Department of Physics

Dean of the Graduate School

I understand that my thesis will become part of the permanent collection of Oregon State University libraries. My signature below authorizes release of my thesis to any reader upon request.

Justin Lee Elser, Author

ACKNOWLEDGEMENTS

Academic

I am indebted to my advisor Dr. Viktor A. Podolskiy for his patience in teaching me.

Personal

I wish to thank my wife Jamie, for following me to Corvallis after she finished her degree. My family for years of their support, and to my advisor.

TABLE OF CONTENTS

TABLE OF CONTENTS (Continued)

LIST OF FIGURES

ELECTROMAGNETIC PROPERTIES OF ANISOTROPIC PLASMONIC METAMATERIALS

1. INTRODUCTION

In recent years engineering advances have made it possible to fabricate materials with features at the micro- or nano-scale[1]. The physics, and specifically the optical properties, of such newly manufactured materials is the focus of this work. With the advent of such fine structure control, several new applications have been developed, including negative index of refraction materials (NIMs) [1, 2, 3], subdiffraction sensors [2], subdiffraction imaging, subwavelength light guiding, propagation of long range surface plasmons [4], planar, super, and hyper-lenses [3, 5, 6]. Other applications include optical cloaks, photonic crystals, and optical computers [7, 8, 9]

The second chapter is a description of 2D Surface Optics. The goal of the surface optic paradigm is to have a complete analogue to 3D ray optics through the use of lenses, prisms, etc..., such that all light is confined to a 2 dimensional plane. This chapter will introduce the concept of the Surface Plasmon Polariton (SPP), an electromagnetic wave that is confined to the interface between materials with opposite in sign dielectric permittivity. Basic properties of these surface waves will be derived, followed by a description and solution of one of the two main problems that exist when trying to use these SPPs in devices. The first problem is that of parasitic scattering that is encountered when an SPP undergoes a change in refraction, such as at the interface between two SPP supporting structures. A method for overcoming this limitation will be discussed, as well as numerical and analytical results showing how effective this method is at minimizing, or in the ideal case, eliminating the scattering. The second problem, that of the SPP not propagating for long distances, will be discussed briefly in §3. In the course of an analytical approach of describing

[1] In optics and this thesis, size is determined by the wavelength size. Micro-scale refers to objects that are between 10^{-3}m and 10^{-6}m, while nano-scale is smaller than micro-scale down to 10^{-9}m. Also, 10^{-6}m is commonly referred to as a *micron*.

the SPP system, mode matching and a matrix expansion technique will be discussed.

Chapter 3. discusses the approaches used to describe a nano-layered system. The Effective Medium theory will be introduced in this section, followed by the exact Transfer Matrix Method, and a non-local correction to the effective medium theory will be shown. It will be shown that the conventional effective medium theory is incapable of describing systems where the change in dielectric permittivity from layer to layer is large. The Transfer Matrix Method will be introduced as an exact analytical method for the solution of the electromagnetics of such systems, but it will be shown that calculation in this manner increases in complexity and computational time as the number of layers is increased. I will show that a non-local correction to the method employed in the effective medium technique will increase the accuracy of the computationally easy effective medium theory.

The last chapter will be a discussion of the more complex system composed of nano-wires. Again, the effective medium theory for this system will be derived. Here it will be shown that the relation of the field inside the wire is not as simply related to the external field as in the layered system. This relationship will be derived, and again confirmed using numerical simulations.

It should be noted that there are actually two types of Surface Plasmons, a quasi-static, localized, non-propagating type simply called a surface plasmon, and the propagating type known as the polariton described above. The standing wave surface plasmon will be described in the chapter on nano-wires as that is an example of a system where it is this form that is relevant.

1.1 Metamaterials

A metamaterial is a synthetic material that has features on the order of optical wavelengths, or smaller. The key feature of metamaterials is that the characteristic size is much smaller than the operating wavelength, $d \ll \lambda$. It is only at this range in which the metamaterial behaves as a homogeneous material so that properties such as an effective index of refraction accurately describe the material. Metamaterials often have periodic structure and hence have much in common with photonic crystals, described in §3.3.2.1. However, photonic crystals generally have periodicity on the same order as the same wavelength, and so usually can not be described by homogenization methods such as effective medium theory.

The most common application of metamaterials is to create materials that exhibit negative index of refraction, which will be discussed in §1.2.1. Other applications include super- [2, 5] and hyper-lenses [6], and recently, cloaking devices [10]. The superlens is a lens that can resolve an image below the diffraction limit. The diffraction limit can be understood in the following way; an infintesimal dipole radiates an electromagnetic field of frequency ω. The electric component of the field can be assumed to be given by a 2D Fourier expansion

$$\vec{E}(\vec{r},t) \propto \sum_{A,k_x,k_y} \vec{E}_A(k_x,k_y)e^{ik_x x+ik_y y+ik_z z-i\omega t} \tag{1.1}$$

where the z axis coincides with the axis of the lens. By applying Maxwell's Equations (see Eq. 1.9) we see that the relation between the components of the wavevector is given by

$$k_z = +\sqrt{\frac{\omega^2}{c^2} - (k_x^2 + k_y^2)} \tag{1.2}$$

Only for the components where k_z is real does the lens apply its phase correction and reassemble the components at the focus. When $\frac{\omega^2}{c^2} < k_x^2 + k_y^2$, the components are decaying and described as evanescent. These evanescent waves can not be recovered by the lens and the so the maximum resolution is given by

$$\Delta \approx \frac{2\pi}{k_{\max}} = \frac{2\pi c}{\omega} = \lambda \tag{1.3}$$

This defines the diffraction limit as the maximum resolution possible by a lens to be $\sim \lambda$. The superlens can beat this by using a metamaterial with $\epsilon = \mu = -1$, which results in a negative index of refraction with $n = -1$ (see §1.2 for details). If the material has this property, the evanescent fields are amplified and there is no phase decay, so the evanescent fields are recovered. However, as was pointed out in Ref. [5], small deviations from $n = -1$ strongly affect the performance of the superlens. Adding absorption, for example, causes this deficiency.

The hyperlens is a metamaterial similar to the superlens but does not have the issue with absorption causing the evanescent fields to be difficult to detect with conventional optics. The hyperlens utilizes anisotropic permittivities in a manner similar to those described in this work but in a cylindrical structure. It can be shown that this geometry magnifies the subwavelength features so that the features are propagating and above the diffraction limit at the output of the lens, which can in turn be imaged via conventional optics.

Cloaking devices are an exciting new application whereby utilizing plasmonics, it is possible to bend light in such a way that it is completely reformed on the other side of the object so that anything inside the object is invisible. This has been demonstrated in microwave frequencies [11], and very recently for optical wavelengths [7]. However, these materials currently can only be created for a single frequency of light. In other words, it may be invisible to red light, but not to green or any other color. Creating a broadband cloak is currently being worked on. Another limitation is that since the light is bent around the object, it is also impossible to "see" anything from inside the cloak at the invisibility frequency. However, this does have incredible applications in the use of stealth technology where the radar system is single frequency and the pilots do not need to use the same frequency to be able to fly.

It is only recently that these materials have been possible to fabricate because of advances in micro- and nano-engineering. The features of these metamaterials can take many forms such as periodic holes in an array, split ring resonators, nanolayers, and nanowires. The periodic hole system can be designed to create photonic crystals, while the split ring resonators can be used for Negative Index of Refraction Materials, described in §1.2.

This work is mostly focused on the material properties of the nanolayered and nanowire structures. The nanolayered structure can be fabricated using techniques such as physical vapor deposition and molecular beam epitaxy. Physical vapor deposition is a process where a material, usually a dielectric but possibly a metal, is superheated until it vaporizes, or more commonly, is subjected to an electron beam which "kicks" the atoms from the material to a gaseous phase. At this point the vapor is allowed to condense onto the surface of the substrate. It does so evenly such that a thin layer has been deposited. Control of thickness of this layer is possible by manipulation of how long the process is allowed. The rate of deposition can be as low as 1 nm/min to a few microns/min. Molecular beam epitaxy is similar in that the material to be deposited is heated in an effusion cell, where it is allowed to sublimate. This material is then allowed to condense onto the substrate. The beam refers to that the molecules do not interact with each other until they reach the substrate due to their long mean free path.

The nanowire structure can be grown with a metal-organic vapor phase-epitaxy technique [12]. In this technique, islands of imperfection are loaded on the substrate. The vapor deposition process will grow where these islands are located, so it is possible to grow the nanowires.

Another technique for creating nanowires is by utilizing a chemical solution [13]. In this method, the nanowires are electrochemically grown in a porous template. The template is made porous by the use of a sulfuric acid electrolyte and then filled in with Au. The template is then chemically etched away, leaving the gold nanowires.

1.1.1 Effective Medium Theory

An Effective Medium Theory (EMT) is an analytical technique that attempts to calculate bulk properties of a medium, usually a metamaterial, by knowing some microscopic properties, such as relative volume fraction and the permittivities of the constituent media. There are several variations of EMT, but two common approaches are that of Maxwell-Garnett and Bruggeman [14] [15] for 3D spheroids. The Maxwell-Garnett approach is used in Ch 4. and is applicable when the volume filling fraction is low [16][17]. Under such conditions, it is further assumed that the field in the medium is homogeneous. Typically, the effective permittivity is then calculated by dividing the average $\vec{D}$ field by the average $\vec{E}$ field, $\epsilon_{\text{eff}} = \frac{\langle D \rangle}{\langle E \rangle}$. More details of these calculations will be explained in §3.3.1. The advantage of the approach of Maxwell-Garnett is that this theory works well for low concentrations. The disadvantage is that it only works for relatively small concentrations.

In contrast, the Bruggeman EMT uses the probability that a given point has one of two permittivities. It then uses Mie theory [18] to calculate the effective conductivity of the medium [14]. The main advantage of the Bruggeman approach is that it works for all concentrations, it is not limited to the small concentrations required by the Maxwell-Garnett theory. However, for metal inclusions in a dielectric host, Bruggeman does not produce as accurate results. Specifically, it does not show the plasmonic resonance used as the basis for much of this presented work.

For layered materials the form of the effective medium is a bit more straightforward. The effective permittivity can again be calculated using the average displacement and electric fields, but is not limited to small concentrations. It does still have the limitation that the characteristic size of the system must be much smaller than the wavelength. This will be explored in detail in §3.3.1 and §3.3.3.

1.1.2 Anisotropy

Anisotropy is a general term meaning that some property is directionally dependent. In this work, it is to be understood that the dielectric permittivity is anisotropic. For linear dielectrics, the permittivity is related to the electric susceptibility χ_e in the equation relating polarization and electric field [19]

$$\mathbf{P} = \hat{\chi}_e \mathbf{E} \tag{1.4}$$

For this work it will be convenient to use the Gaussian units in which the permittivity of free space is unitary, $\epsilon_0 = 1$. The Heaviside-Lorentz units are the same as the cgs (Gaussian) units, except for a factor of $\sqrt{4\pi}$ in the definitions of the fields and the electric charge. There is a similar relation for the magnetic permeability and magnetization

$$\mathbf{M} = \hat{\chi}_m \mathbf{H} \tag{1.5}$$

The relationship between χ_e and ϵ is given by the dimensionless definition

$$\epsilon \equiv (1 + 4\pi\chi_e). \tag{1.6}$$

To explicitly define the anisotropic nature of the dielectric permittivity, the permittivity can be expressed as a tensor. In this work, $\hat{\epsilon}$ will be used when referring to the tensor:

$$\hat{\epsilon} = \begin{pmatrix} \epsilon_{xx} & \epsilon_{xy} & \epsilon_{xz} \\ \epsilon_{yx} & \epsilon_{yy} & \epsilon_{yz} \\ \epsilon_{zx} & \epsilon_{zy} & \epsilon_{zz} \end{pmatrix} \tag{1.7}$$

while ϵ will be understood to refer to a scalar permittivity. For most systems, the coordinate system can be chosen such that Eq. 1.7 becomes diagonal

$$\hat{\epsilon} = \begin{pmatrix} \epsilon_{xx} & 0 & 0 \\ 0 & \epsilon_{yy} & 0 \\ 0 & 0 & \epsilon_{zz} \end{pmatrix} \tag{1.8}$$

This condition of diagonality will be assumed for this work.

Optically anisotropric materials exist in naturally occuring forms. This is what causes certain materials, such as calcite, to be birefringent. The birefringence is due to the permittivity

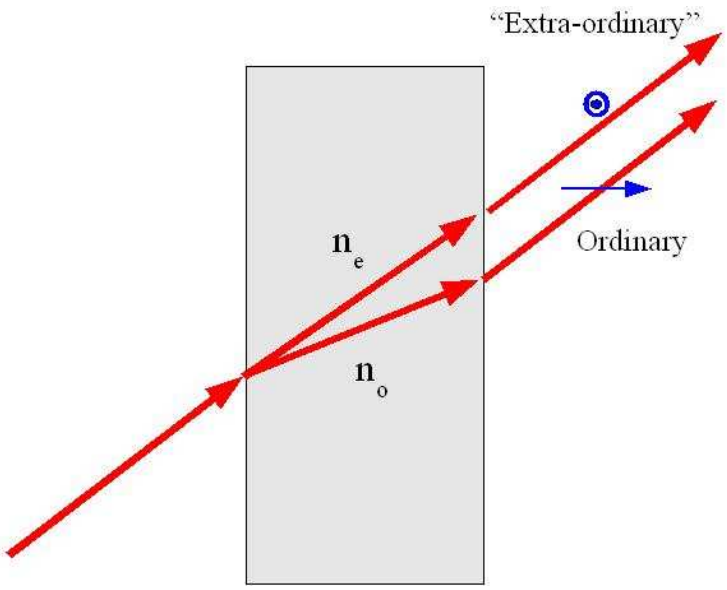

FIGURE 1.1: Drawing of a birefringent slab of material. The birefringence causes the ordinary and extraordinary waves to refract at different angles.

felt by one polarization of light to be different than that of the other polarization. In the literature, the polarizations are commonly referred to as ordinary and extraordinary polarizations. Fig. (1.1) shows how the different polarizations are affected by the birefringence.

In materials such as calcite, the birefringence is due to the crystal structure. In a sense, the lattice length (lattice constant) is compressed in a coordinate direction from the length in other directions. Because this length is different, the interaction of the electromagnetic wave with the atoms in the crystal will be altered differently in the different directions. In a material that has two similar directions for the anistropy, it is referred to as uniaxial. The axis about which there is rotational symmetry in a uniaxial material is called the optical axis. Materials in which all three directions are anisotropic are called biaxial and have two axes of anistropy.

1.2 Negative Index of Refraction Materials

1.2.1 Overview

Materials that have simultaneously negative dielectric permittivity and magnetic permeability were described by Veselago [1] in 1968 to exhibit a negative index of refraction. A negative

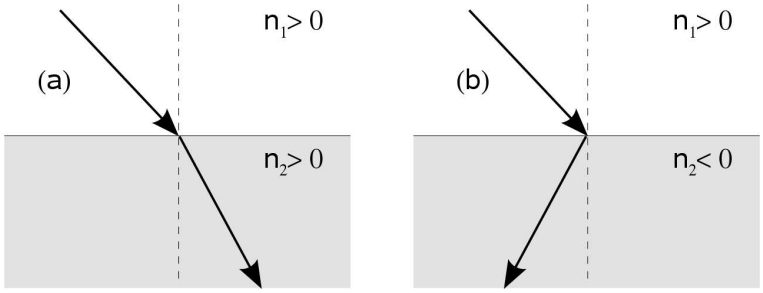

FIGURE 1.2: (a) The refraction of light at an interface with positive index of refraction. (b) Refraction at the interface between a positive to negative index.

index of refraction means that light that is incident is refracted on the *same* side of the normal as the incident ray, as illustrated in Fig. (1.2). This can result in wide range of new physics topics such as planar lenses, reversed Doppler effect and a reversed Cherenkov radiation.

To describe the theory, some background materials must be developed first. We begin with Maxwell's equations, which in Gaussian units are

$$\begin{aligned} \vec{\nabla} \times \vec{E} + \frac{1}{c}\frac{\partial \vec{B}}{\partial t} &= 0 \\ \vec{\nabla} \times \vec{H} = \frac{1}{c}\left(\frac{\partial \vec{D}}{\partial t} + 4\pi\vec{J}\right) & \\ \vec{\nabla} \cdot \vec{D} &= 4\pi\rho \\ \vec{\nabla} \cdot \vec{B} &= 0 \end{aligned} \tag{1.9}$$

For the purposes of this work, $\vec{J} = 0$. The electric field $\vec{E}$ and the magnetic flux density $\vec{B}$ are vectors, and $\vec{D}$ and $\vec{H}$ are given by

$$\begin{aligned} \vec{D} &= \vec{E} + 4\pi\vec{P} = \hat{\epsilon}\vec{E} \\ \vec{B} &= \vec{H} + 4\pi\vec{M} = \hat{\mu}\vec{H} \end{aligned} \tag{1.10}$$

where $\vec{P}$ is given by Eq. (1.4), $\vec{M}$ by Eq. (1.5). Also, $\hat{\mu}$ is defined in a similar manner to $\hat{\epsilon}$ in §1.1.2, but for the magnetic susceptibility χ_m. In the case of isotropic media, the tensors for dielectric permittivity and magnetic permeability become diagonal with three identical entries. The tensors can then be replaced with the scalars ϵ and μ. Together, Eqs. (1.9, 1.10) completely describe the propagation of electromagnetic waves within a medium. By taking the curl of $\vec{\nabla} \times \vec{E} + \frac{1}{c}\frac{\partial \vec{B}}{\partial t} = 0$,

and using the definition in Eq. (1.10), one obtains the wave equation

$$\nabla^2 \vec{E}(\vec{r},t) = \frac{\epsilon\mu}{c^2}\frac{\partial^2 \vec{E}(\vec{r},t)}{\partial t^2} \tag{1.11}$$

where $c = 2.9979 \times 10^{10}$cm/s is the speed of light in vacuum. The wave equation has solutions $\propto f(\pm(\vec{k}\cdot\vec{x} - \omega t))$. For convenience, the plane wave solution of $f = e^{\pm i(\vec{k}\cdot\vec{x}-\omega t)}$ is used as the derivatives and integrals involving the exponential function are simple. For the plane wave solution, the phase velocity is given by $\nu_{ph} = \omega/k = c/n$ where n is the index of refraction for the propagating wave. Plugging this information into Eq. (1.11)

$$k^2\vec{E} = \frac{\epsilon\mu\omega^2}{c^2}\vec{E} \tag{1.12}$$

Using the definition $n = c/\nu_{ph}$, we find that

$$n = \pm\sqrt{\epsilon\mu} \tag{1.13}$$

For a hand-waving argument to show how a negative index of refraction is possible from the above equation, we separate the terms, where we see that $n = \sqrt{\epsilon}\sqrt{\mu}$, where if ϵ and μ are both negative, we obtain a factor of $i^2 = -1$, leading us to the conclusion that this determines the sign for n. Other causal arguments can also be discussed directly from Maxwells' Equations by adding a small absorption term to the permittivity. If this is done, in order to ensure causality that the energy dissipates as the wave travels through the medium, the negative root must be the correct one. If all signs of permittivity and permeability are tabulated, we can create a quadrant map of the signs for ϵ and μ to determine what type of material would be formed, as illustrated in Fig. (1.3).

There are no known naturally occuring materials that have simultaneously negative permittivity and and permeability. In 1999, it was suggested by Pendry [20] that metamaterials may be able to meet this condition if fabricated properly. The specific design that was proposed was that of split-ring resonators (SRR), as illustrated in Fig. (1.4 a).

According to Ref. [20], the effective permeability for the SRR is

$$\mu_{\text{eff}} = 1 - \frac{\pi r^2}{a^2}\left(1 + i\frac{2\sigma}{\omega r\mu_0} - \frac{3dc_0^2}{\pi^2\omega^2 r^3}\right)^{-1} \tag{1.14}$$

where r is the radius of the outer ring, a is the distance to the nearest neighboring split ring (center to center), σ is the resistance of the cylinder surface per unit area (assumed to be small),

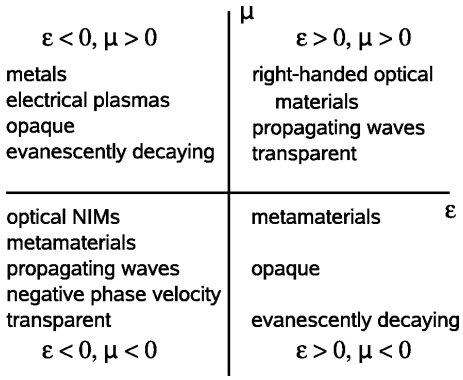

FIGURE 1.3: Quadrant map showing how the sign of permittivity and permeability determine the reflection and refraction properties of a material.

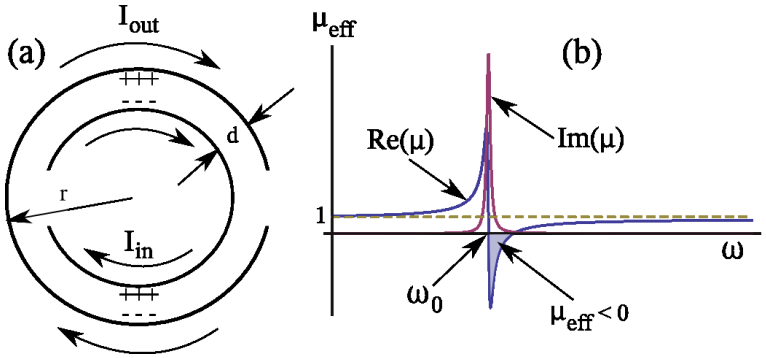

FIGURE 1.4: The Split Ring Resonator (SRR). (a) A magnetic field perpendicular to the plane of the rings induces currents in the wire. (b) The resonant condition for the permeability creates a region where the permeability is negative. The negative permittivity is from the wires being metallic.

and d is the distance separating the rings, illustrated in Fig. (1.4 a). As seen in Fig. (1.4 b), this produces a resonance at a frequency ω_0, where for slightly higher frequencies a negative effective permeability is found. While this does allow for simultaneously negative effective permeability and permittivity, it has the drawback that the negative permeability only occurs in a small range of frequencies near the resonance. As is the case with most resonant conditions, the absorption is extremely large in the region near the resonance, as evidenced by the large imaginary part shown in the figure. Therefore, although it is possible to achieve the negative index materials with this configuration, the performance suffers from large losses due to the absorption.

Another issue is the size of manufacturing such systems to obtain negative refraction in freqencies near optical. To obtain high frequencies (small wavelength), the size of the split ring must be small. The first structures to be designed with the split-ring design could only be made such that the negative region was in the microwave (GHz) frequencies. With advances in fabrication techniques, it has been possible to scale down the negative refraction to THz region, but this is still short of the goal of negative refraction at optical or infrared frequencies. Overcoming this shortcoming is the subject of the following section.

1.2.2 Non-Magnetic Anisotropic NIMs

The negative index in anisotropic metamaterials [21] is possible in a 2D planar waveguide by implementing a new parameter ν to replace the magnetic permeability μ in the dispersion relation

$$k_x^2 + k_y^2 + k_z^2 = \epsilon\mu k^2 \tag{1.15}$$

In the case of a 2D anisotropic waveguide structure as illustrated in Fig. (1.5 a), the TM wave would have electric and magnetic fields

$$\begin{aligned} E &= \left\{ i\frac{k_z^2 + k_y^2}{k_z\kappa^2}\frac{\epsilon_{yz}}{\epsilon_x}E_0';\ \frac{k_y}{k_z}E_0;\ E_0 \right\} \\ H &= \left\{ 0;\ i\frac{k\epsilon_x}{\kappa^2}E_0';\ -i\frac{kk_y\epsilon_x}{k_z\kappa^2}E_0' \right\} \end{aligned} \tag{1.16}$$

where $k = \omega/c$, and prime (') means differentiation with respect to x. The field can be written as $E_0(x, y, z, t) = E_0(x)e^{-i\omega t + ik_y y + ik_z z}$ from the equation

$$E_0'' + \kappa^2 E_0 = 0 \tag{1.17}$$

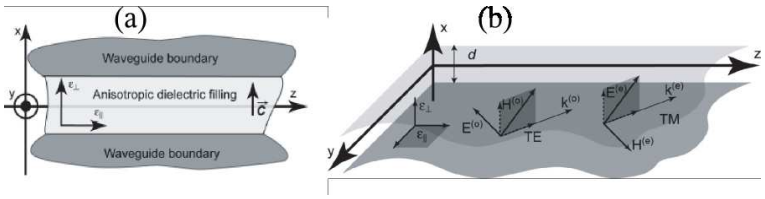

FIGURE 1.5: (a) Schematic drawing of the 2D anisotropic waveguide structure to create non-magnetic negative index of refraction. (b) Drawing of the TE and TM field vectors. Notice that for TE modes, the electric field is in the $y-z$ plane and thus $\epsilon_\perp$ is not in the dispersion relation.

with the conventional boundary conditions for the tangential (y,z) components of the electric field at the waveguide walls. For the rest of the following derivation, perfectly conducting walls will be assumed.

The solutions to Eq. (1.17) are a series of modes given by $E_0(x) = A_m \cos \kappa x$ with $\kappa = (2m+1)\pi/d$ and $E_0(x) = A_m \sin \kappa x$ with $\kappa = 2m\pi/d$ where m is an integer.

Each waveguide mode than has its own dispersion relation

$$k_y^2 + k_z^2 = \epsilon_x \nu k^2 \tag{1.18}$$

where $\nu = 1 - \frac{\kappa^2}{\epsilon_{yz} k^2}$. The parameter κ defines the mode structure in the x direction. The anisotropy in the waveguide is "felt" only by the TM modes because as seen in Fig. (1.5), the electric field has no component in both the parallel and perpendicular direction for the TE mode. In this waveguide structure ϵ_x and ϵ_{yz} can be independently controlled, thus it is possible to have a simultaneously negative ϵ_x and ν.

From Eq. (1.18) it is seen that a propagating solution (when k_y and k_z are both real) can only exist in systems where ϵ_x and ν are of the same sign. The case where $\epsilon_x > 0; \nu > 0$ would give a similar result to that of an isotropic while the case of $\epsilon_x > 0; \nu < 0$ would give that of a sub-critical waveguide where no propagating modes exist and all incident radiation would be reflected. The case of $\epsilon_x < 0; \nu > 0$ also would not support propagation and would behave as a waveguide with a metallic core. Finally, the case where $\epsilon_x < 0; \nu < 0$ would support propagating waves, but to verify that the waves exhibit negative refraction the sign of the phase velocity must be shown to be negative.

While Eq. (1.18) determines the magnitude of the phase velocity $v_p = \omega/(k\sqrt{\epsilon_x \nu})$, it can not give the sign of the phase velocity. The material can be defined to be left-handed (negatively

refracting) if the phase velocity is negative. For simplicity, it is assumed that the propagating TM polarized wave is normal to the waveguide, ie. along the z-direction as shown in Fig. (1.5). In this case, $H_z = H_x = 0$ and $k_y = 0$, where from Eq. (1.16) we find that $H_y = (k\epsilon_x/k_z)E_x$. To enforce the boundary condition of tangential H at the interface between an isotropic right-handed material and the anisotropic metamaterial, k_z and ϵ_x must be of the same sign. Thus, if ϵ_x is negative so is k_z, so the phase velocity is also negative.

For the more general case of oblique incidence, it can be shown via numerical 3D calculations (see Ref. [21]), that by assuming that absorption occurs away from the interface (in other words, the field decays away from the interface), that the phase velocity is also negative for the case of $\nu < 0; \epsilon_x < 0$.

1.3 Conclusion

We have shown some of the background physics behind effective medium theories, dielectric anisotropy, and negative index of refraction materials, including a method to achieve left-handedness via anisotropic metamaterials.

The following chapter will expand on these ideas by introducing the concept of Surface Plamson Polaritons, a unique case of electromagnetic surface wave propagation. The chapter will also describe a fundamental problem with these surface waves of scattering at an interface and introduce an approach to overcome this limitation utilizing anisotropic metamaterials.

The last two chapters separately show two different geometries that can be manufactured to exhibit anisotropy. The first is a nanolayered structure made by alternating layers of different materials. The second is a nanowire based system where the wires are arranged so that they are parallel to each other in a host material.

2. 2D SURFACE OPTICS

2.1 Intro

Surface Plasmon Polaritons (SPPs) [22] are electromagnetic surface waves that exist at the boundary between materials with opposite sign in dielectric permittivity. This surface wave is highly confined to the surface and so can be used as the enabling mechanism for subdiffraction sensing, imaging, and subwavelength light guiding [23, 24, 25, 26, 27, 28, 29, 30, 31, 32]. One disadvantage to surface waves is that they suffer from a parasitic scattering between surface optic elements with a change in index of refraction. This scattering can be understood to be caused by the mismatch in k-vector caused by the change in index of refraction. Because the mode is not matched, all other possible k-vector modes are excited in an effort to make up the difference. These new modes are bulk free-space modes that exist in the constituent materials. The loss is dependent on the magnitude of the change in index, but as much as 30% of the incident wave energy is radiated away in free space modes at a single boundary.

The focus of this chapter is to derive an approach to be used to calculate the reflection, transmission, and scattering coefficients in such a system. This chapter also describes a method utilizing anisotropic metamaterials to minimize and under certain conditions, eliminate this parasitic scattering.

Note that another type of surface wave known as a D'yakonov wave can exist at the interface between an isotropic and an anisotropic dielectric [33]. However, the geometry of such a system must be more complicated than what will be described below as for such a wave to exist, the optic axis must not be perpendicular to the interface.

Also, discussion in this work will be limited to SPPs that exist due to opposite in sign permittivity, but SPPs also exist at interfaces with opposite in sign magnetic permeability [34]. There is a direct mapping between dielectric permittivity and magnetic permeability, as can be seen from the symmetrical equations in the introduction. Replacing ϵ with μ and TM with TE in this work will result in similar physics. This work will focus on permittivity as it is generally easier to manipulate, but it should be noted that all results can be obtained in a similar manner for the case of permeability. Moreover, for the rest of this work, the relative magnetic permeability will

assumed to always be $\mu_r = 1$ for nonmagnetic materials.

2.2 Surface Plasmon Polaritons

SPPs are transverse magnetic (TM) solutions of Maxwells equations propagating at the interface between materials with opposite signs of dielectric permittivity. They are a result of the coupling between the oscillations of the electrons at the surface of a conductor and an electromagnetic wave.

As will be seen below, the properties of the SPP are completely described by the permittivities of the two materials involved. Thus, control of the SPP can be achieved via adjustion of the permittivities by techniques such as corrugation of the surface, a change in substrate, or changing the permittivity directly by deposition [23, 24, 25, 26, 27, 28, 29, 30, 31, 32].

2.2.1 Dispersion relation for Surface Plasmon Polaritons

Derivation of the dispersion relation for SPPs is done via the standard wave matching technique. The geometry of the structure is illustrated in Fig. (2.1 a), and consists of a dielectric (Region 1) and metallic (Region 2) medium separated at the $x = 0$ plane. The premise is that a surface wave would exist at the interface $x = 0$. If the wave is confined to this surface, the field must be damped at $x \to \pm\infty$. Since we are assuming TM modes, the field is expressed in terms of the magnetic field in each region as

$$\begin{aligned} H_{1y} &= H_0 e^{ik_z z - \kappa_1 x - i\omega t} \quad x > 0 \\ H_{2y} &= H_0 e^{ik_z z + \kappa_2 x - i\omega t} \quad x < 0 \end{aligned} \tag{2.1}$$

where we have assumed $k_y = 0$ as the coordinates can be rotated so that there is only propagation in the z direction. Note that $\kappa = ik_x$. With this information, we can solve for $\kappa_{1,2}$ by the use of Eq. (1.15)

$$\kappa_{1,2} = \sqrt{k_z^2 - \frac{\omega^2 \epsilon_{1,2}}{c^2}} \tag{2.2}$$

The boundary condition at $x = 0$ are that tangential $\vec{E}$ and $\vec{H}$ are continuous. The condition for H_y only yields what we already knew, that k_z must be the same on both sides. To find the

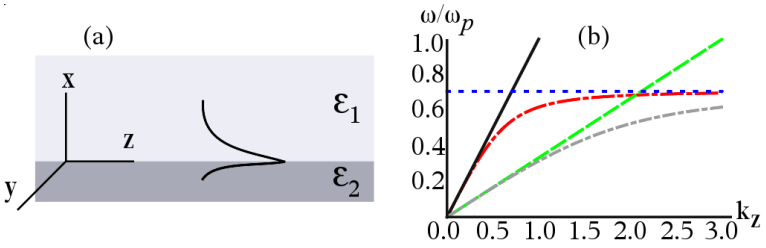

FIGURE 2.1: (a) Schematic of the plasmon supporting structure. The interface is at $x = 0$ and the SPP propagates in the $y - z$ plane. The decay profile of the SPP is also shown, note that the SPP decays much more rapidly in the metal region due to $|\epsilon_2| \gg \epsilon_1$. (b) Dispersion relation plots for various surface waves. The solid line is the dispersion relation for light in vacuum, long dashed-dotted line is the derived dispersion for an SPP at a vacuum-metal interface, straight dashed line is light in a medium with $\epsilon = 3$, and the short dashed-dotted line is SPP dispersion with $\epsilon_1 = 3$ with the same metal. The dashed line shows the asymptotic maximum supported freqency at $\omega/\omega_p = \sqrt{2}$. ω_p is the plasma frequency given by $\sqrt{\frac{4\pi ne^2}{m}}$.

condition for E_z, we can use Ampere's Law to find it in terms of H_y.

$$\vec{\nabla} \times \vec{H} = \frac{1}{c}\frac{\partial \vec{D}}{\partial t} = \frac{\epsilon}{c}\frac{\partial \vec{E}}{\partial t} \Rightarrow \frac{\partial E_z}{\partial t} = \frac{c}{\epsilon}\frac{\partial H_y}{\partial x} \tag{2.3}$$

After evaluating the derivatives and evaluating at $x = 0$, Eq. (2.3) reduces to

$$\frac{-\kappa_1}{\epsilon_1} = \frac{\kappa_2}{\epsilon_2} \tag{2.4}$$

Upon substitution of Eq. (2.2) and some algebra, the final result is obtained

$$k_z^2 = \frac{\omega^2}{c^2}\frac{\epsilon_1\epsilon_2}{\epsilon_1 + \epsilon_2} \tag{2.5}$$

Note that attempting the same approach using TE modes will not be successful as the boundary condition for H_z can not be satisfied for $\kappa_1 \neq \kappa_2$. Also, the materials must be opposite in sign in terms of dielectric permittivity so that Eq. (2.4) can be satisfied.

From the definition of n defined earlier, we can describe an "effective" index of refraction

$$n_{\text{eff}} = k_z c/\omega = \sqrt{\frac{\epsilon_1\epsilon_2}{\epsilon_1 + \epsilon_2}} \tag{2.6}$$

This effective index of refraction completely describes the propagation of the surface plasmon.

The dispersion relation for various propagating surface waves is shown in Fig. (2.1 b). It can be seen that it is impossible to directly excite the SPP solely at the vacuum-metal interface

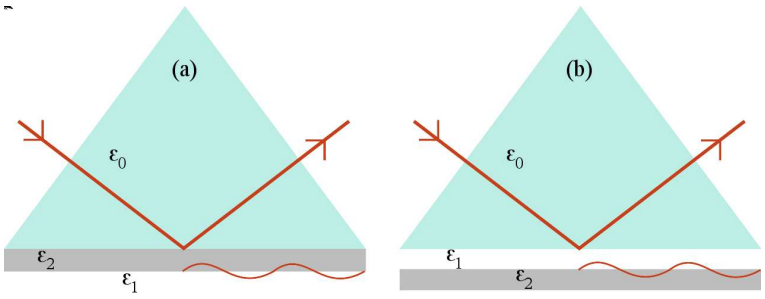

FIGURE 2.2: Configurations to excite SPPs. (a) The Kretschmann configuration, the plasmon is excited on the metallic surface away from the prism. The metal strip must be thin so that the energy can evanescently decay through to the side where the wavevector can be matched as described in the text. (b) The Otto configuration, similar to the Kretshcmann, but instead has a small gap between the prism and the metal strip.

with a plane wave because the dispersion curves never cross, except at $\omega = 0$, implying that there is no way to match the momentum wavevector. To be able to match the momentum, light is passed through a prism with a larger index of refraction. This prism will have a thin strip of metal either attached to the underside of the prism (known as the Kretschmann configuration), or separated by a small gap from the prism (known as the Otto configuration), illustrated in Fig. (2.2). The Kretschmann configuration is more commonly used because it is easier to manufacture and to observe the plasmon.

One important use for the surface plasmon is that of Surface Plasmon Resonance (SPR). This is commonly used in biology and other sciences to accurately determine the index of refraction of small particles, including molecules. The basic idea is that the Kretschmann configuration is used where the particle to be detected is placed on the metallic strip. The light through the prism is swept through a range of angles while measuring the amount of light that is observed in the output of the prism. The intensity of the output will drop dramatically when the wavevectors are matched and most of the energy is in the SPP instead of being reflected through the prism. This process is called Attenuated Total Reflection. By measuring the angle where the minimum occurs, it is possible to calculate the permittivity of the particle through the use of Eq. (2.5)

The above derivations were all done in the case of isotropic permittivity. The case of anisotropic permittivity will be done in §(2.3).

2.3 Description of Scattering Problem

It is possible to control the propagation of SPPs by fabrication techniques so that the index of refraction can be changed. For example, corrugating the surface or simply by having different dielectrics deposited on a metallic substrate. However, this degree of control comes at a price in that when a change in n_{eff} occurs, a simultaneous change in spatial decay profile κ_j also happens due to their interdependence in Eq. (2.5). Since κ is related to k_x, for the system to be conserved, all possible modes (or k_x) values are excited to make up for the difference. This can be understood to be from the Fourier series needing an infinite number of terms in the series to approximate the curve that it would have been if there was no mismatch. These excited modes are a series of free-space modes that radiate away with wavevector for anisotropic TM waves

$$k^2 = \frac{\omega^2}{c^2} = \frac{k_x^2}{\epsilon_{yz}} + \frac{k_y^2 + k_z^2}{\epsilon_x} \tag{2.7}$$

An SPP that experiences a change in index of refraction will in fact excite a set of scattered plane waves in addition to reflected and transmitted SPPs. This is in contrast to plane waves, where only the reflected and transmitted plane waves are excited. This is due to the fact that for plane wave refraction, there exists a translational symmetry which requires that the $(\vec{k}_1 \cdot \vec{x})_{z=0} = (\vec{k}_{1r} \cdot \vec{x})_{z=0} = (\vec{k}_2 \cdot \vec{x})_{z=0}$, where $\vec{k}_{1r}$ is the reflected wave vector. This is the basis for the Law of Reflection (since $k_{1x} = k_{1xr}$) and for Snell's Law. Since a change in index of refraction for the SPP system requires a minumum of 3 materials, there is no symmetry and thus no condition that the wavevector component must be the same everywhere at the boundary.

For any appreciable change in effective index in the SPP system, 10%-30% of the total energy is scattered away as plane waves. The reduction in intensity is not however, the only problem. Another effect this scattering has is that of coupling between the surface and plane waves. When this coupling occurs it can have an undesirable interference with the surface mode. Fig. (2.3) shows the parasitic scattering caused by the change in refractive index.

We will now derive the above dispersion relation, Eq. (2.7), with Maxwell's equations. We use the two equations involving the curl of the fields from Eq. (1.9) with no free currents ($\vec{J} = 0$)

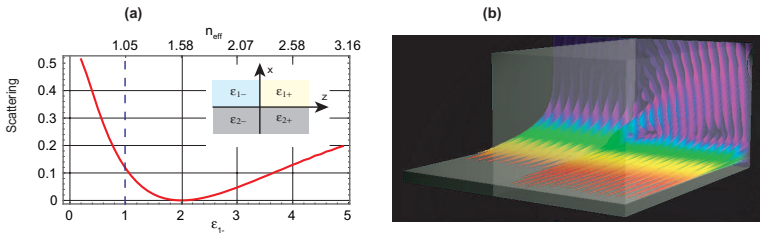

FIGURE 2.3: (a) Fractional energy scattered away as free-space plane waves from an SPP undergoing a change in index of refraction. Inset is a schematic of structure. (b) Plot of H_z field showing the scattering of plane waves away from the point of intersection of materials.

and noting that for plane waves these reduce to

$$\begin{aligned} \vec{k} \times \vec{E} &= \frac{\omega}{c}\vec{H} \\ \vec{k} \times \vec{H} &= -\frac{\omega}{c}\hat{\epsilon}\vec{E} \end{aligned} \tag{2.8}$$

By solving for $\vec{H}$ in the first equation and substituting into the second, we obtain

$$\vec{k} \times \vec{k} \times \vec{E} = -\frac{\omega^2}{c^2}\hat{\epsilon}\vec{E} \Rightarrow k^2\vec{E} - \vec{k}(\vec{k} \cdot \vec{E}) - \frac{\omega^2}{c^2}\hat{\epsilon}\vec{E} = 0 \tag{2.9}$$

Putting this into a matrix form assuming the material is uniaxial

$$\begin{pmatrix} k^2 - k_x^2 - \frac{\omega^2}{c^2}\epsilon_x & -k_x k_y & -k_x k_z \\ -k_x k_y & k^2 - k_y^2 - \frac{\omega^2}{c^2}\epsilon_{yz} & -k_y k_z \\ -k_x k_z & -k_x k_z & k^2 - k_z^2 - \frac{\omega^2}{c^2}\epsilon_{yz} \end{pmatrix} \begin{pmatrix} E_x \\ E_y \\ E_z \end{pmatrix} = 0 \tag{2.10}$$

For this to have a non-trivial solution, the determinant of the matrix must $= 0$. Evaluating the determinant yields

$$\left(k^2 - \frac{\omega^2}{c^2}\epsilon_x\right)\left(k_x^2\frac{\omega^2}{c^2}\epsilon_{yz} + (k_y^2 + k_z^2)\frac{\omega^2}{c^2}\epsilon_x - \frac{\omega^4}{c^4}\epsilon_x\epsilon_{yz}\right) \tag{2.11}$$

Leading to the dispersion relation for TE waves

$$k^2 = k_x^2 + k_y^2 = k_z^2 = \frac{\omega^2}{c^2}\epsilon_x \tag{2.12}$$

and for TM waves

$$\frac{\omega^2}{c^2} = \frac{k_x^2}{\epsilon_{yz}} + \frac{k_y^2 + k_z^2}{\epsilon_x} \tag{2.13}$$

2.4 Derivation of effective index for SPPs in an anisotropic medium

Now that we have derived the anisotropic dispersion relation, we can derive the analogue to Eq. (2.5) for an SPP in an anisotropic medium [35]. This can be achieved by analyzing the behavior of the surface waves by deriving the propagation properties and the spatial profile of an SPP at the interface between two uniaxial media with tensorial permittivities $\hat{\epsilon}_1$ and $\hat{\epsilon}_2$. We represent the field inside the materials as

$$\vec{\mathbb{E}} = \begin{cases} a_1\vec{E_1}, & x > 0 \\ a_2\vec{E_2}, & x < 0 \end{cases} \qquad (2.14)$$

$$\vec{\mathbb{H}} = \begin{cases} a_1\vec{H_1}, & x > 0 \\ a_2\vec{H_2}, & x < 0 \end{cases}$$

with

$$\begin{aligned} \vec{E_1} &= \left\{ \frac{c}{\omega}\frac{k_y^2+k_z^2}{\epsilon_1^x}, \frac{c}{\omega}\frac{i\kappa_1 k_x}{\epsilon_1^{yz}k_z}, -\frac{c}{\omega}\frac{i\kappa_1 k_x}{\epsilon_1^{yz}k_z} \right\} e^{-i\omega t-\kappa_1 x+ik_y y+ik_z z} \qquad (2.15) \\ \vec{E_2} &= \left\{ \frac{c}{\omega}\frac{k_y^2+k_z^2}{\epsilon_2^x}, \frac{c}{\omega}\frac{i\kappa_2 k_x}{\epsilon_2^{yz}k_z}, -\frac{c}{\omega}\frac{i\kappa_2 k_x}{\epsilon_2^{yz}k_z} \right\} e^{-i\omega t+\kappa_2 x+ik_y y+ik_z z} \\ \vec{H_1} &= \left\{ 0, 1, -\frac{k_y}{k_z} \right\} e^{-i\omega t-\kappa_1 x+ik_y y+ik_z z}, \\ \vec{H_2} &= \left\{ 0, 1, -\frac{k_y}{k_z} \right\} e^{-i\omega t+\kappa_2 x+ik_y y+ik_z z}, \end{aligned}$$

and a_1 and a_2 being (unknown) field amplitudes. As it can be explicitly verified, thus selected fields $(\vec{E_1}, \vec{H_1})$ and $(\vec{E_2}, \vec{H_2})$ satisfy Maxwell equations in the regions 1 and 2 respectively [21], and enforce harmonic in-plane propagation and exponential out-of-plane decay of SPP. The components of the wavevector in $(\vec{E_j}, \vec{H_j})$ are related through Eq. (2.13):

$$-\frac{\kappa_j^2}{\epsilon_j^{yz}} + \frac{k_y^2+k_z^2}{\epsilon_j^x} = \frac{\omega^2}{c^2}.$$

To find the propagation properties of the SPP it remains to satisfy the boundary conditions at the interface $x = 0$. Taking into account identical field distribution in $y - z$ plane, these are reduced

to:

$$\begin{aligned} a_1 &= a_2 \\ -a_1\kappa_1\frac{1}{\epsilon_1^{yz}} &= a_2\kappa_2\frac{1}{\epsilon_2^{yz}}. \end{aligned} \tag{2.16}$$

The non-trivial solutions of Eq.(2.16) exist only when

$$k_y^2 + k_z^2 = K^2 = \frac{\omega^2}{c^2}\frac{\epsilon_1^x\epsilon_2^x(\epsilon_1^{yz} - \epsilon_2^{yz})}{\epsilon_1^x\epsilon_1^{yz} - \epsilon_2^x\epsilon_2^{yz}}, \tag{2.17}$$

The isotropic version of this equation ($\epsilon_j^x = \epsilon_j^{yz}$) yields Eq.(2.5).

Together Eqs.(2.16,2.16,2.17) provide complete information about structure and propagation properties of the SPP mode.

2.5 Minimizing Scattering

To eliminate the out of plane scattering, it is sufficient to meet two conditions. These are that the spatial profile κ is independent of the refractive index, and that there is no interpolarization (TE $\leftrightarrow$ TM) coupling. Both conditions are satisfied when

$$\kappa_{1-}^2 = \kappa_{1+}^2, \quad \kappa_{2-}^2 = \kappa_{2+}^2 \Rightarrow \frac{\epsilon_{1+}^x}{\epsilon_{1-}^x} = \frac{\epsilon_{2+}^x}{\epsilon_{2-}^x}, \quad \epsilon_{1-}^{yz} = \epsilon_{1+}^{yz}, \quad \epsilon_{2-}^{yz} = \epsilon_{2+}^{yz} \tag{2.18}$$

where "-" denotes the left side ($z < 0$) of the system, while "+", the right side ($z > 0$).

Therefore, the ideal scattering free plasmonic optical system has constant in-plane (ϵ^{yz}) components of the permittivity tensor, while the out of plane (ϵ^x) components are free to change as long as the ratio constraint in Eq. (2.18) is met.

Because the in-plane permittivity does not change, the structure is completely transparent to TE polarized radiation, from which it is evident that TE waves do not scatter at the interface and hence do not couple back to any TM waves.

When there is no scattering, the calculation of parameters such as reflected and refracted amplitudes (a_t, a_r) of the E_1^x component, and refraction angles becomes the same as that of the more familiar 3D optics, namely that of the Fresnel equations:

$$\frac{a_r}{a_i} = \frac{k_{z-} - k_{z+}}{k_{z-} + k_{z+}}, \quad \frac{a_t}{a_i} = \frac{2k_{z-}}{k_{z-} + k_{z+}} \tag{2.19}$$

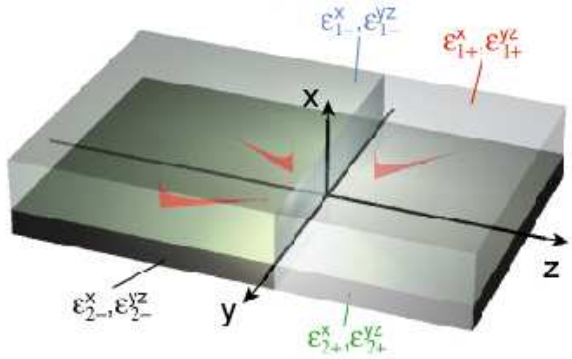

FIGURE 2.4: Schematic of anisotropic SPP supporting structure

and Snell's law

$$n_- \sin(\theta_i) = n_- \sin(\theta_r) = n_+ \sin(\theta_t) \tag{2.20}$$

To show that the conditions in Eq. (2.18) are sufficient to have no scattering, we numerically solve Maxwell's Equations for a SPP supporting structure that undergoes a change in index of refraction. The system is illustrated in Fig (2.4) and is composed of two connected SPP structures. The first structure is that of a metamaterial with $\epsilon_{1-}^{x} = 2.7$ and $\epsilon_{1-}^{yz} = 1$ for the dielectric region, and an isotropic metallic medium with $\epsilon_2 = -10$. These media would correspond to an silver-silica composite and silver at a vacuum wavelength of 500 nm. The structure on the right side would be composed of vacuum for the dielectric and a $\epsilon_{2+}^{x} = -3.71; \epsilon_{2+}^{yz} = -10$ which could be constructed from an aluminium-gold layered structure as described in [36] [37].

To verify that this is indeed scattering free, Maxwell's equations were solved numerically via Mathematica (this program neglects scattering). The components of the electric and magnetic fields are shown in Figs. (2.5 2.6). Since the components of the tangential electric and magnetic and normal displacement fields are seen to be matched on both sides of the interface, the proposed solution satisfies Maxwell's equations. From the uniqueness theorem [19], since this solution works, it must be *the* solution. In other words, if there was scattering in this system, the boundary conditions would not have been satisfied.

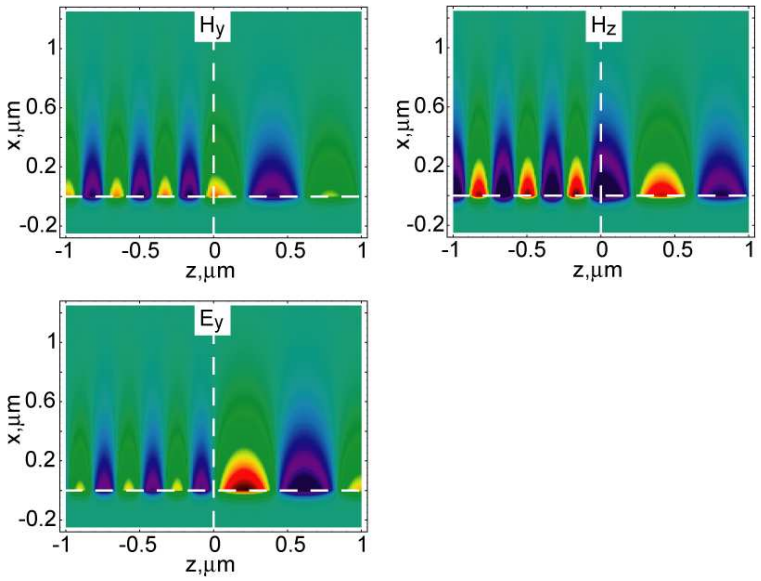

FIGURE 2.5: Continous components of the field with a $y = 0$ crossection

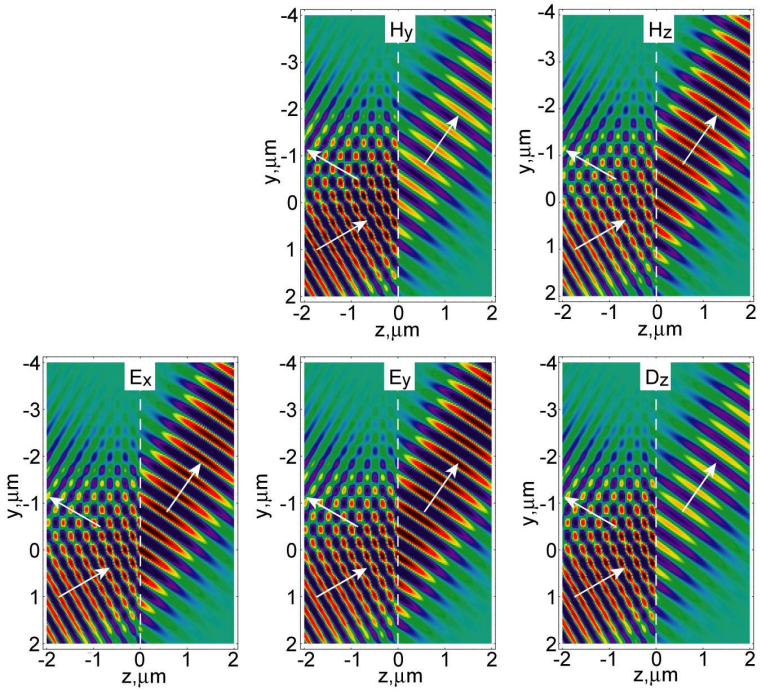

FIGURE 2.6: Continous components of the field with a $x = 50nm$ crossection

2.6 Volume modes in the four media SPP structure

The total field in the four media structure (illustrated in Fig. 2.4) will be the sum of the field due to the SPP and all possible volume modes on each side of the interface at $z = 0$. Thus, the electric field with field incident from $-x$ would be

$$\begin{aligned} \vec{E}_{-}^{inc} + \int r_1(\vec{k_1})\vec{E}_{-}(\vec{k_1})d\vec{k_1} + \int r_2(\vec{k_2})\vec{E}_{-}(\vec{k_2})d\vec{k_2} \\ = \int t_1(\vec{k_1})\vec{E}_{+}(\vec{k_1})d\vec{k_1} + \int t_2(\vec{k_2})\vec{E}_{+}(\vec{k_2})d\vec{k_2} \end{aligned} \tag{2.21}$$

where the 1 and 2 subscripts denote modes in the dielectric and metallic regions, respectively, and r and t are the reflection and transmission coefficients yet to be found.

Each volume mode is a propagating wave described by three components, the incident, reflected and transmitted waves. A set of volume modes exists in each of the four different materials. We will see that the volume modes in the dielectric media will dominate, but for completeness (and to satisfy boundary conditions), volume modes in the metal regions should be included. For the purposes of this work, the incident amplitude of the H_y^{inc} component of the field is assumed unitary, and $k_y = 0$ is assumed for simplification. Thus, the total magnetic field for the TM wave can be expressed as

$$\vec{H} = \begin{cases} \{0,1,0\}\left(e^{-ik_{1x}x} + \rho e^{ik_{1x}x}\right) & x > 0 \\ \{0,1,0\}\,\tau e^{-ik_{2x}x} & x < 0 \end{cases} \tag{2.22}$$

where the harmonic spatial and temporal dependence $e^{ik_z z - i\omega t}$ has been assumed the same for all fields, and so has been factored out. Using Ampere's Law, it is found that $\vec{E} = \left\{\frac{k_{jz}c}{\epsilon_x \omega}, 0, \frac{-k_{jx}c}{\epsilon_{yz}\omega}\right\} H_y$. It should be noted that since k_{2x} can be found using the relation $k_{2x} = \sqrt{\epsilon_2^{yz}\left(\frac{\omega^2}{c^2} - \frac{k_z^2}{\epsilon_2^x}\right)}$, which involves a square root, ensuring causality requires a complex plane cut along the negative imaginary axis so that $\arg[k_{2x}] \in \left(-\frac{\pi}{4}, \frac{3\pi}{4}\right]$. The amplitude coefficients ρ and τ can be calculated via the standard wave matching techniques to obtain the well-known equations

$$\begin{aligned} \rho &= \frac{k_{1x}\epsilon_2^{yz} - k_{2x}\epsilon_1^{yz}}{k_{1x}\epsilon_2^{yz} + k_{2x}\epsilon_1^{yz}} \\ \tau &= \frac{2k_{1x}\epsilon_2^{yz}}{k_{1x}\epsilon_2^{yz} + k_{2x}\epsilon_1^{yz}} \end{aligned} \tag{2.23}$$

As mentioned earlier, we allow for the case where the the incident radiation is from the metallic side. In this case, the volume magnetic field is

$$\vec{H} = \begin{cases} \{0,1,0\}\,\tau e^{ik_{1x}x} & x > 0 \\ \{0,1,0\}\left(e^{ik_{2x}x} + \rho e^{-ik_{2x}x}\right) & x < 0 \end{cases} \tag{2.24}$$

resulting in reflection and transmission coefficients

$$\begin{aligned} \rho_M &= \frac{k_{2x}\epsilon_1^{yz} - k_{1x}\epsilon_2^{yz}}{k_{2x}\epsilon_1^{yz} + k_{1x}\epsilon_2^{yz}} \\ \tau_M &= \frac{2k_{2x}\epsilon_1^{yz}}{k_{2x}\epsilon_1^{yz} + k_{1x}\epsilon_2^{yz}} \end{aligned} \tag{2.25}$$

For completeness, note that the TE modes can be analyzed similarly. A schematic of the open-waveguide system showing just the volume modes incident from the dielectric is illustrated in Fig. (2.7 a). Note that for a complete picture for Fig. (2.7 b), the modes incident from the metal must be included on both sides of the vertical and horizontal interfaces.

2.7 Analytical Approximation to calculate coefficients

In this section, we will derive expressions for calculating reflection, transmission, and scattering coefficients. We start with a description of mode orthogonality followed by the mode matching technique.

2.7.1 Orthogonality

The set of SPP and possible volume modes described in the previous sections that can exist in an SPP supporting structure make up a complete and orthogonal set of eigenmodes [38] [39]. Because of their completeness, mapping of the eigenmode expansions on either side of a change in refractive index or other discontinuity is possible. This will allow for the use of a numerical method outlined by Clarricoats [40] and with which Oulton [39] applied to the case of surface waves, although it was applied with the assumption the modes incident from the metal region were negligable. We will show later that this assumption is incorrect under certain conditions.

Mathematically, the orthogonality condition is

$$\int\int_{-\infty}^{\infty} \vec{E}(\vec{r};\vec{k}) \times \vec{H}^{\dagger}(\vec{r};\vec{k'}) \cdot \hat{z} dx dy = N\delta(\vec{k} - \vec{k'}) \tag{2.26}$$

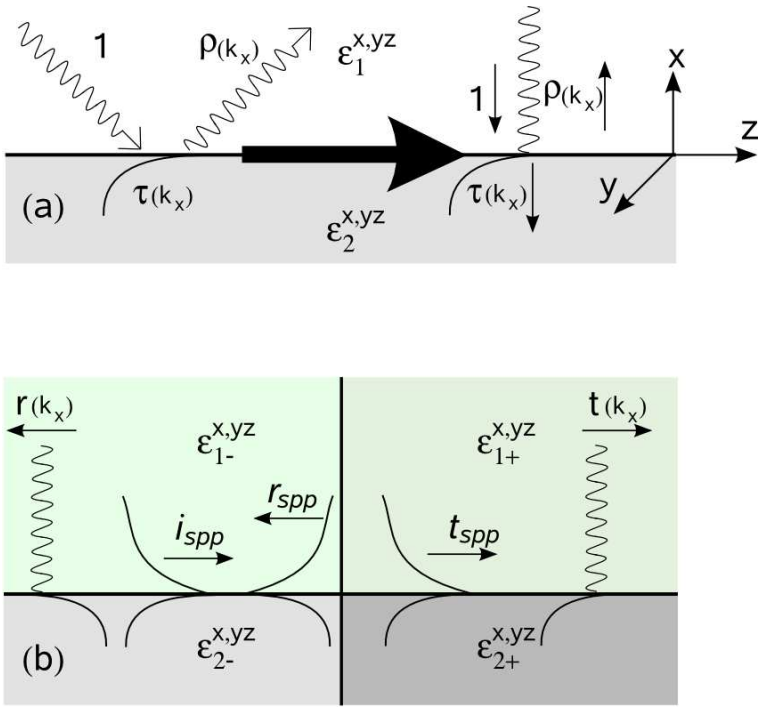

FIGURE 2.7: Schematic of the open waveguide structure. (a) The incident light has magnitude 1 and has reflection and transmission coefficients given by ρ and τ. The right side shows a shorthand notation to describe the volume modes. (b) The full system has an incident, reflected and transmitted SPP as well as the set of reflected (from the $z = 0$ interface) and transmitted volume modes. Note that the mirror image of this picture is needed to account for the volume modes incident from the metal side (bottom).

where $\vec{E}, \vec{H}$ are the electric and magnetic fields in a region (must be the same region), and N is some normalization that is calculated from earlier definitions. In other words, if the fields are in the same region, but have different modes determined by their wavevectors $\vec{k}$ and $\vec{k'}$, the cross product of the electric and magnetic fields yields 0. However, if they do have the same modal profile, the result of Eq. (2.26) is non-zero.

An example calculation of the orthogonality condition can be done by assuming the fields both have a plane wave type field given by

$$\left\{\vec{E}, \vec{H}\right\} \propto e^{i\vec{k}\cdot\vec{r}} \tag{2.27}$$

Applying the cross and dot products would give (to within a normalization factor)

$$e^{i(\vec{k}-\vec{k'})\cdot r} \tag{2.28}$$

Integrating this expression from $-\infty$ to ∞ is the definition of a Fourier transform integral, the result of which is a delta function.

2.7.2 Mode Matching

The mode matching technique is a way to single out the contribution of a given mode. But first, a more detailed description of the geometry of the system under consideration is needed. Fig. (2.4) shows a detailed view. The SPP is assumed to propagate in $z-$direction with the horizontal interface separating the dielectric and metal materials being at $x = 0$. The vertical interface where the change in index of refraction occurs is at $z = 0$. We will use the notation that $(-|+)$ will give the negative and positive z materials respectively, while $(1|2)$ will denote the dielectric and metal materials.

For an example of the mode matching technique, the total field modes on both sides $(-|+)$ can be described with Eq. (2.21)

$$\vec{E}_{-}^{inc} + \int r_1(\vec{k_1})\vec{E}_{-}(\vec{k_1})d\vec{k_1} + \int r_2(\vec{k_2})\vec{E}_{-}(\vec{k_2})d\vec{k_2} = \int t_1(\vec{k_1})\vec{E}_{+}(\vec{k_1})d\vec{k_1} + \int t_2(\vec{k_2})\vec{E}_{+}(\vec{k_2})d\vec{k_2}$$

where $r_{1,2}$ and $t_{1,2}$ are intensity reflection and transmission coefficients for a given $\vec{k}$ for the dielectric and metallic incident volume modes, respectively. Post vector crossing this with $\vec{H}_{-}(\vec{k}_i)\cdot\hat{z}$

and integrating over all x would give the coupling coefficient of the i^{th} mode of $\vec{k}$. This coupling coefficient would be from the result of an overlap integral. The overlap integral is a measure of how much the wavefunctions of the different fields overlap, similar to what is seen in quantum mechanics.

As an example calculation of this technique, let us derive the coupling coefficient for the case of a dielectric volume mode on the $(-)$ side coupled to another dielectric volume mode on the $(+)$ side of the interface. The coefficients r and t are to be derived. Note that ρ and τ are defined along the x-axis, while r and t are along the z-axis, so the integrals must be split at $x = 0$.

Then, the mode matching technique can be expressed mathematically as

$$\begin{aligned}\left\langle \vec{E}_+(\vec{k}_+), \vec{H}_-(\vec{k'}_-) \right\rangle &= \int_{-\infty}^{\infty} \vec{E}_+(\vec{k}_+) \times \vec{H}_-(\vec{k'}_-) \cdot \hat{z} dx \\ &= \int_0^{\infty} \left(\frac{k_{1+z}c}{\epsilon_{1+x}\omega} e^{-ik_{1+x}x} + \rho_+ \frac{k_{1+z}c}{\epsilon_{1+x}\omega} e^{ik_{1+x}x} \right) \left(e^{-ik'_{1-x}x} + \rho_- e^{ik'_{1-x}x} \right) dx \\ &+ \int_{-\infty}^{0} \tau_+\tau_- \frac{k_{2+z}c}{\epsilon_{2+x}\omega} e^{-i(k_{2+x}+k'_{2-x})x} dx\end{aligned} \tag{2.29}$$

This integral is trivial to integrate once it is noticed that $\int_0^{\infty} e^{\pm ikx} dx = \int_{-\infty}^{\infty} \Theta(x) e^{\pm ikx} dx$ is just a Fourier transform of the Heaviside Theta function, $\Theta(x)$, the result of which is $\pi\delta(k) \pm \frac{i}{k}$. The end result of this calculation, after noting that several of the delta functions disappear because the direction has already been taken into account, is

$$\begin{aligned}\left\langle \vec{E}_+(\vec{k}_+), \vec{H}_-(\vec{k'}_-) \right\rangle &= \frac{k_{z+}c}{\omega} \left[\frac{\rho_+ + \rho_-}{\epsilon_{1x+}} \pi\delta(k_{1x+} - k'_{1x-}) + \frac{\rho_+\rho_- - 1}{\epsilon_{1x+}} \frac{i}{k_{1x+} + k'_{1x-}} \right. \\ &+ \left. \frac{\rho_+ - \rho_-}{\epsilon_{1x+}} \frac{i}{k_{1x+} - k'_{1x-}} + \frac{\tau_+\tau_-}{\epsilon_{2x+}} \frac{i}{k_{2x+} + k'_{2x-}} \right]\end{aligned} \tag{2.30}$$

Similar expressions can be found by looking at the coupling for the case of $\left\langle \vec{H}_+(\vec{k}_+), \vec{E}_-(\vec{k'}_-) \right\rangle$ and also for the cases involving the metal incident modes. Altogether, a total of sixteen integrals can be found by applying this technique.

2.7.3 Matrix Expansion

The incident, reflection, and transmission amplitude coefficients can be related to all fields in the system in a general matrix form of Eq. (2.21):

$$\begin{aligned}\hat{I}_E \vec{i} + \hat{R}_E \vec{r} &= \hat{T}_E \vec{t} \\ \hat{I}_H \vec{i} + \hat{R}_H \vec{r} &= \hat{T}_H \vec{t}\end{aligned} \tag{2.31}$$

where E and H denote Electric and Magnetic fields, respectively. In this formalism, $\hat{I}_{E,H}$ represents a normalization matrix from the incident amplitudes. The $\hat{R}_{E,H}$ and $\hat{T}_{E,H}$ matrices are formed from overlap integral calculations described above. In particular, define the $(1,1)$ elements of the matrices to be that of the SPP-SPP coupling coefficients. For example, $\hat{T}_{E_{11}}$ would correspond to the overlap between the incident magnetic field of the SPP and the electric field of the SPP on the transmitted side, or, in the notation of Eq. (2.29),

$$\hat{T}_{E_{11}} = \left\langle \vec{E}_+(k_{spp}), H_-(k_{spp}) \right\rangle \tag{2.32}$$

Continuing this definition, (1,m) and (m,1) represent the SPP-volume and volume-SPP overlaps, and (m,m) the volume-volume overlaps

$$\begin{aligned} \hat{T}_{E_{1m}}(k_x) &= \left\langle \vec{E}_+(k_x), \vec{H}_-(\vec{k_{spp}}) \right\rangle \\ \hat{T}_{H_{m1}}(k_x) &= \left\langle \vec{H}_+(\vec{k_{spp}}), \vec{E}_-(k_x) \right\rangle \\ \hat{T}_{E_{mm}}(k_x) &= \left\langle \vec{E}_+(k_x), \vec{H}_-(k_x) \right\rangle \end{aligned} \tag{2.33}$$

and all possible combinations as described in the previous section. Note that since these expressions are part of the integral in Eq. (2.21) they must be multiplied by $d\vec{k}$ as a weight factor.

Also, $\vec{i}$,$\vec{r}$, and $\vec{t}$ are vectors given by $\langle i_{spp}, 0\rangle$, $\langle r_{spp}, (\rho_-, \tau_-)(k_x)\rangle$, and $\langle t_{spp}, (\rho_+, \tau_+)(k_x)\rangle$, where ρ and τ are reflection and transmission amplitude coefficients for a volume mode described by k_x as defined by Eq. (2.23).

By solving Eq. (2.31) for $\vec{r}$ and $\vec{t}$, taking care to keep the proper order of the matrix multiplications, we obtain:

$$\begin{aligned} \vec{r} &= -\left(\hat{T}_E^{-1}\hat{R}_E - \hat{T}_H^{-1}\hat{R}_H\right)^{-1}\left(\hat{T}_E^{-1}\hat{I}_E - \hat{T}_H^{-1}\hat{I}_H\right)\vec{i} \\ \vec{t} &= \left(\hat{R}_E^{-1}\hat{T}_E - \hat{R}_H^{-1}\hat{T}_H\right)^{-1}\left(\hat{R}_E^{-1}\hat{I}_E - \hat{R}_H^{-1}\hat{I}_H\right)\vec{i} \end{aligned} \tag{2.34}$$

Because the quantity we are looking for is the total amount of energy scattered away and not that of a particular mode, we only need the reflection and transmission intensity values (R and T) of the SPP. As such, we only require knowing the 1^{st} elements of $\vec{r}$ and $\vec{t}$. Knowing these, the scattering can be calculated as $S = 1 - R - T$, where $R = |r|^2, T = |t|^2 \frac{S_+^{\text{flux}}}{S_-^{\text{flux}}}$ with S^{flux} being the Poynting flux. Also, because individual modes are orthogonal on the same side of the interface,

matrices $\hat{I}$ and $\hat{R}$ are diagonal. Moreover, by calculating these matrix elements, it can be shown that $\hat{I}_E = \hat{I}_H = \hat{R}_H = -\hat{R}_E$. This simplifies Eq. (2.34) to

$$\begin{aligned} \vec{r} &= \hat{R}_H^{-1}\left(\hat{T}_E^{-1} + \hat{T}_H^{-1}\right)^{-1}\left(\hat{T}_E^{-1} - \hat{T}_H^{-1}\right)\hat{I}_E\vec{i} \\ \vec{t} &= 2\left(\hat{T}_E + \hat{T}_H\right)^{-1}\hat{I}_E\vec{i} \end{aligned} \tag{2.35}$$

Because $\hat{T}_{E,H}$ are not a diagonal matrices, there is some difficulty in calculating the inverse of such an infinite matrix. However, in the limit that scattering is weak, these matrices are *nearly* diagonal, ie. the non-diagonal elements are much smaller than those of the diagonal. In this case, a general matrix

$$\hat{M} = \begin{pmatrix} M_{11} & M_{12} & \cdots \\ M_{21} & M_{22} & \cdots \\ \vdots & \vdots & \ddots \end{pmatrix} \tag{2.36}$$

can be separated into a diagonal matrix $\tilde{M}$ and non-diagonal part $\bar{M}$ such that $\hat{M} = \tilde{M}\left(\hat{1} + \bar{M}\right)$. Then

$$\begin{aligned} \hat{M}^{-1} &= \left[\tilde{M}\left(\hat{1} + \bar{M}\right)\right]^{-1} \\ &= \left(\hat{1} + \bar{M}\right)^{-1}\tilde{M}^{-1} \end{aligned} \tag{2.37}$$

and by using a Taylor series expansion

$$\left(\hat{1} + \bar{M}\right)^{-1} \approx \left(\hat{1} - \bar{M} + \bar{M}^2\right) \tag{2.38}$$

Therefore, for an individual matrix element;

$$\hat{M}_{ij}^{-1} = \frac{1}{M_{ii}}\left(\delta_{ij} - \frac{M_{ij}(1-\delta_{ij})}{M_{ii}} + \sum_{k\neq i}\frac{M_{ik}M_{kj}}{M_{ii}M_{kk}}\right) \tag{2.39}$$

Written in the shorthand notation of Eq. (2.33), the above approximation gives for the expressions for $\vec{t}_1$ and $\vec{r}_1$ with a continous wavevector space;

$$\begin{aligned} \vec{t}_1 &= \frac{2I_{E_{11}}}{T_{E_{11}} + T_{H_{11}}}\left(1 + \int \frac{\left[T_{E_{1m}}(k_x) + T_{H_{1m}}(k_x)\right]\left[T_{E_{m1}}(k_x) + T_{H_{m1}}(k_x)\right]}{\left[T_{E_{11}} + T_{H_{11}}\right]\left[T_{E_{mm}}(k_x) + T_{H_{mm}}(k_x)\right]}dk_x\right) \\ \vec{r}_1 &= \left(\frac{T_{H_{11}} - T_{E_{11}}}{T_{H_{11}} + T_{E_{11}}}\right)\left[1 - \beta_{11}^{+} + \beta_{11}^{-} + \alpha_{11}^{+}\right] - \alpha_{11}^{-}\left(\frac{T_{H_{mm}}(k_x) - T_{E_{mm}}(k_x)}{T_{E_{11}} + T_{H_{11}}}\right) \end{aligned} \tag{2.40}$$

with the definitions

$$\beta_{11}^{\pm} = \int \left(\frac{\frac{T_{E_{1m}}(k_x)T_{E_{m1}}(k_x)T_{H_{11}}}{T_{E_{11}}T_{E_{mm}}(k_x)} \pm \frac{T_{H_{1m}}(k_x)T_{H_{m1}}(k_x)T_{E_{11}}}{T_{H_{11}}T_{H_{mm}}(k_x)}}{T_{H_{11}} \pm T_{E_{11}}} \right) dk_x \tag{2.41}$$

$$\alpha_{11}^{\pm} = \int \left(\frac{\frac{T_{E_{1m}}(k_x)T_{H_{11}}}{T_{E_{11}}} + \frac{T_{H_{1m}}(k_x)T_{E_{11}}}{T_{H_{11}}}}{T_{H_{11}} + T_{E_{11}}} \right) \left(\frac{\frac{T_{E_{m1}}(k_x)T_{H_{mm}}(k_x)}{T_{E_{mm}}(k_x)} \pm \frac{T_{H_{m1}}(k_x)T_{E_{mm}}(k_x)}{T_{H_{mm}}(k_x)}}{T_{H_{mm}}(k_x) \pm T_{E_{mm}}(k_x)} \right) dk_x$$

The result of Eq. (2.40) is that we now have expressions to calculate R and T to a second order correction. The much improved agreement this method has for calculating reflection, transmission, and emittance coefficients is seen in Fig. (2.8). Note that for some cases, there is no difference between the uncorrected and corrected results for R and T, but the correction is noticeable in the much smaller magnitude range for S. Also of note is that although the correction may have no noticeable disagreement with R or T, the agreement with S may seem to be less than ideal. Because the magnitude of the value of S can be $3 \sim 4$ orders of magnitude smaller than R or T, but the magnitude of the *absolute* error is roughly the same, the approximation of using only the 2^{nd} order terms in the expansion of the inverse matrices is much more noticeable. Further evidence for the limitation of this approach is that the 3^{rd} order term in the matrix inverse expansion is proportional to the 2^{nd}, so the difference between numerical and analytical results is greater when the corrected calculations are greater, ie. when the correction is visibly different than the uncorrected case.

It should be noted that the above derivation does not take in to account the volume modes in the metallic media. As will be discussed in §2.9, under the condition that the SPP is near resonance ($\epsilon_1 \approx -\epsilon_2$), the coupling with these modes can become non-negligable. Therefore, the above approximation assumes that the matrix is nearly diagonal, which is equivalent to $|\epsilon_2| \gg \epsilon_1$.

The approximation also works for the case of materials with absorption. Fig. (2.9) shows the excellent agreement of numerical and analytical results. However, care must be taken when dealing with absorption so that the sign of $Im(k_x, k_z) > 0$ for passive media [41] [42]. To this end, a careful choice of a branch cut will ensure this result, as discussed in §2.5.

2.8 Numerical Simulations

To analyze the tolerance of this technique to fabrication defects, we analyze the system by using the finite element solver program COMSOL 3.4 [43]. In this program, we designed a system as illustrated in Fig (2.4), and take advantage of the fact that the problem can be simulated in just 2-D. We look at several different cases and calculate the ratio of energy scattered away relative to the incident energy given by $S = 1 - R - T$ where R and T are the reflection and transmission intensity coefficients calculated by COMSOL. These coefficients can be calculated as follows:

$$r = \frac{\int \left(\vec{H}_c - \vec{H}_{\text{inc}}\right) \cdot \vec{E}^*_- dx}{\int \left(\vec{H}_- \cdot \vec{E}^*_-\right) dx} \tag{2.42}$$

$$t = \frac{\int \left(\vec{H}_c \cdot \vec{E}^*_+\right) dx}{\int \left(\vec{H}_+ \cdot \vec{E}^*_+\right) dx} \tag{2.43}$$

where $\vec{H}_c$ is the computed magnetic field at the appropriate region being integrated over, $\vec{H}_{\text{inc}}$ is the calculated incident magnetic field that must be subtracted away to get the contribution due to only the reflection, and integration is done over the particular region of interest, (-) for reflection, and (+) for transmission. These values must then be normalized to the incident power flow, and squared to obtain intensity coefficients R and T.

The results from COMSOL are seen in Fig. (2.8) where a decrease in scattering by a factor of 100 is seen. It is also evident that merely meeting the condition of the first part of Eq. (2.18) that in-plane (ϵ^{yz}) is constant across the interface is enough to dramatically decrease the scattering, even while the second condition that the ratio of out-of-plane permittivity is not strictly held.

2.9 Limitations of the Matrix Expansion and Numerical Simulations

As was mentioned previously, the picture is incomplete without calculating the coupling with the metal incident modes. However, the analytical approximation for the matrix inversion did not take these into account. This can account for some of the discrepency in certain cases between the approximation and the numerical simulations using COMSOL. If the matrix elements are calculated including these extra modes, it is noticed that under certain conditions, the assumption

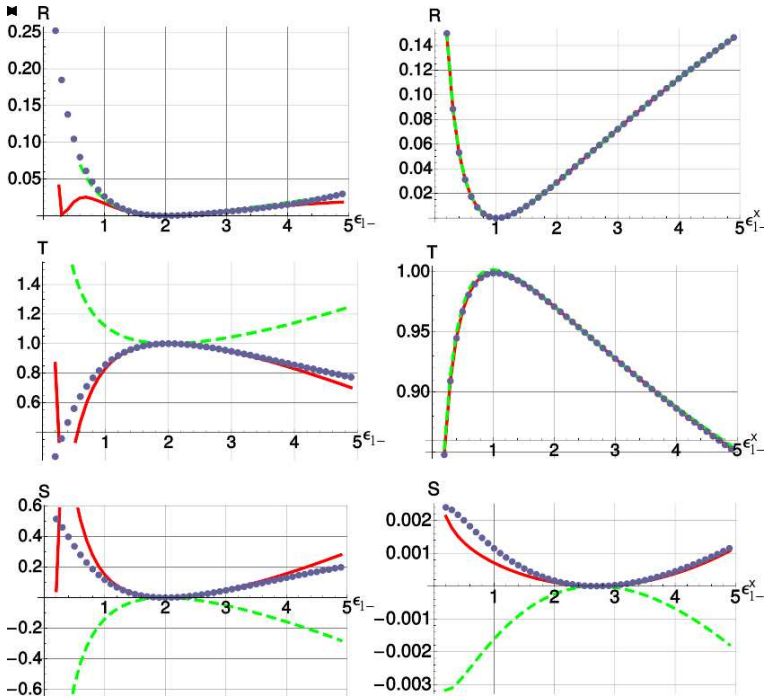

FIGURE 2.8: Results of numerical simulations compared to analytical approximations. Left plots show the reflection, transmission, and scattering coefficients for an isotropic system with $\epsilon_{2+,-} = -10$, $\epsilon_{1+} = 2$ and ϵ_{1-} is varied. Note the relatively large fraction of energy scattered away in this system. Right plots are for an anisotropic system with $\epsilon^{yz}_{1-} = \epsilon^{x,yz}_{1+} = 1$, $\epsilon^{x,yz}_{2-} = \epsilon^{yz}_{2+} = -10$, $\epsilon^{x}_{2+} = -3.71$, and ϵ^{x}_{1-} is varied. Dotted lines are numerical results from Comsol, dashed lines are 1^{st} order approximations for coefficients, while the solid lines are analytical approximations to 2^{nd} order. Note the much higher degree of accuracy for the 2^{nd} order approximation. In fact, the 1^{st} order value for transmission in the isotropic case is clearly wrong as it shows a value > 1, which is only possible in active media. Also note the 100 fold decrease in scattering with the anisotropic metamaterial.

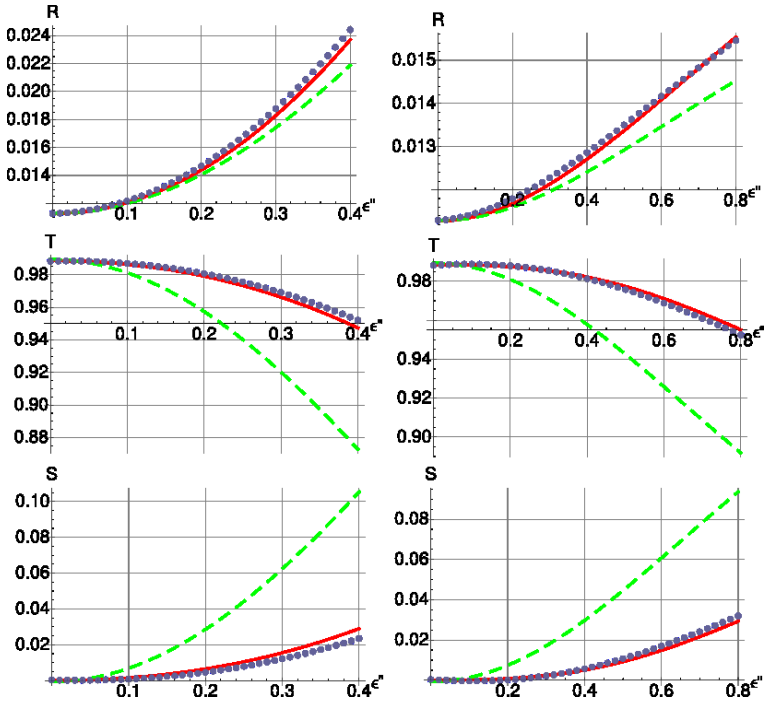

FIGURE 2.9: Results of numerical simulations compared to analytical approximations for the case of absorption. The real part of the permittivity was mode matched according to Eq. (2.18) while absorption was numerically added to the dielectric (Left figures) and the metal (Right figures). The corrected approximation (red solid lines) is clearly superior to the uncorrected (green dashed lines) in matching the numerical results from COMSOL (blue dots).

that the matrix is nearly diagonal is no longer true. This is illustrated in Fig. (2.10). The problematic cases occur when the metal and dielectric permittivities are similar in magnitude

$$\epsilon_{1x,1yz} \approx -\epsilon_{2x,2yz} \tag{2.44}$$

As can be seen in the density plots of Fig. (2.10), the coupling between the dielectric and metal volume modes can sometimes be substantial, thus breaking the condition that the matrix is *nearly* diagonal.

Furthermore, not including the metal modes will show another issue, namely that the boundary condition that tangential $\vec{E}$ and $\vec{H}$ fields are not continuous. Again, for cases where the difference in magnitude of the permittivities is large, this is not as large of an issue because the off -diagonal modes that get excited are much more weakly coupled. This is illustrated in Fig. (2.11).

2.10 Applications

This section will briefly discuss some applications that would benefit from the scattering-free plasmonic systems described above.

2.10.1 Electro-optics

A possible application of the extremely weak scattering SPP system lies in that of electroplasmonics. Electroplasmonics is based on the principles of electro-optics where an applied external electric field can alter the optical effective index of refraction. The permittivity would then be related to the field by the Kerr effect

$$\begin{aligned} \epsilon^{x} &= \epsilon_0^{x} + \alpha \mathbf{E^2} \\ \epsilon^{yz} &= \epsilon_0^{yz} \end{aligned} \tag{2.45}$$

Such power can be utilized to implement tunable surface optical elements. For example, a system can be designed such that when an electric field is applied the permittivity in the x-direction can be altered such that the structure then meets the requirements of Eq. (2.18) so that the surface wave is transmitted through, with negligable loss due to scattering. Such an optical element could be fabricated in to lenses or prisms, as illstrated in Fig. (2.12) to create dynamic elements. The

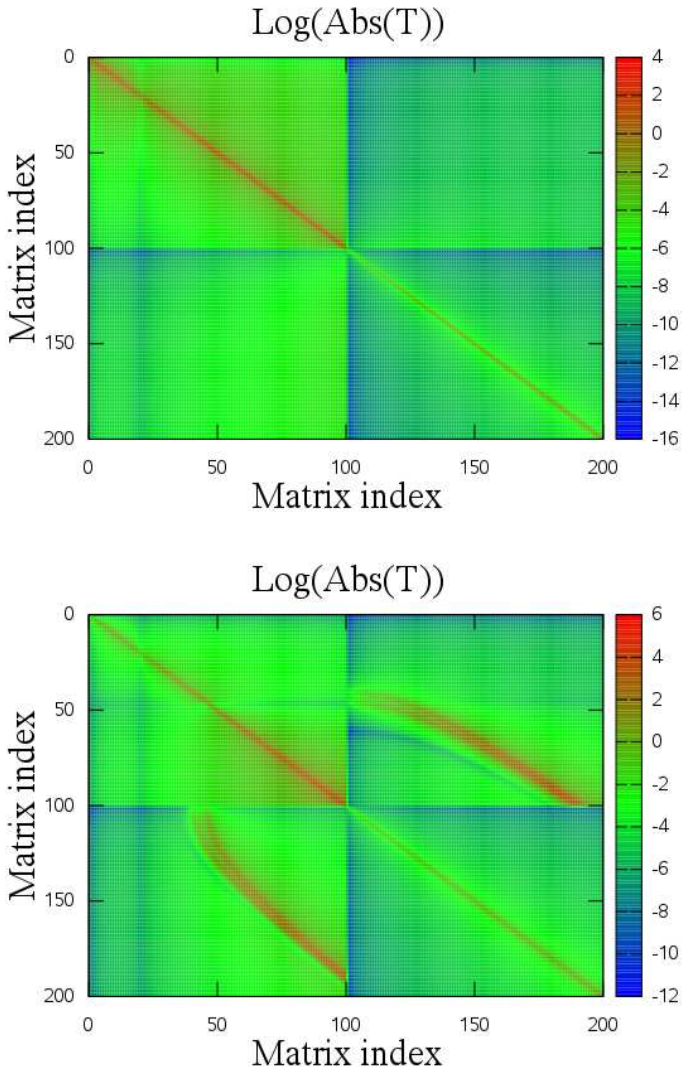

FIGURE 2.10: Density plots of the matrix elements in the $\hat{T}_E$ matrix. Note that the matrix can be separated into four quadrants. The top left quadrant is that of the dielectric volume-dielectric volume mode coupling. The top right and bottom left are the dielectric-metal and metal-dielectric while the bottom right is the metal-metal volume mode couplings. (a) $\epsilon_{1-} = 2.25; \epsilon_{1+} = 1; \epsilon_2 = -28.3 + 0.5i$. (b) $\epsilon_{1-} = 2.25; \epsilon_{1+} = 1; \epsilon_2 = -3 + 0.1i$

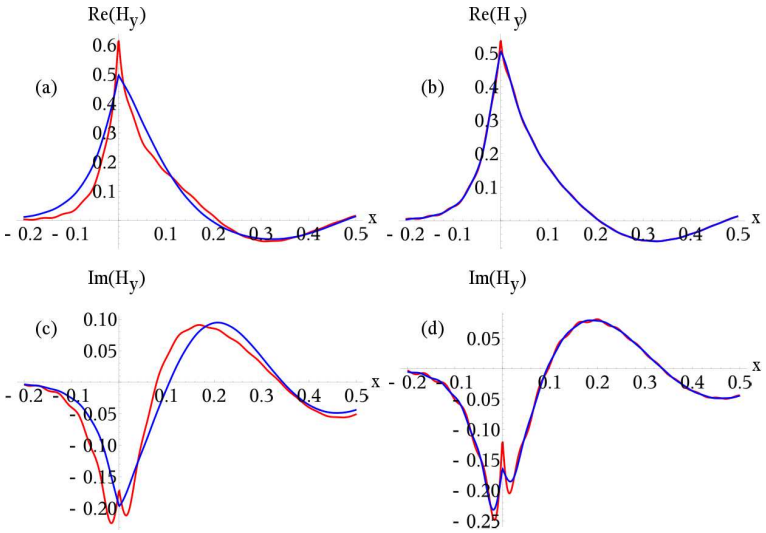

FIGURE 2.11: Comparison of the H_y field at the boundary $z = 0$. (a) and (b) show the real part of H_y, (c) and (d) the imaginary component. (a) and (c) only assume volume modes from the dielectric. (b) and (d) assume all possible combinations of volume modes. The two lines show the field at $z = -0$ and $z = +0$, respectively. Note the convergence when all possible modes are considered.

lens, prism, or band-gap structure could be destroyed simply by changing the external electric field, there is no need for physical modifications.

2.10.2 2D Planar Optics

The approach of utilizing anisotropic metamaterials is not limited to eliminating scattering of surface waves. Indeed, the approach can be generalized to achieve waveguide mode matching in a planar waveguide. The mode matching condition equations (2.18) can be generalized to a form of

$$\begin{aligned} \epsilon^x(x,y,z) = &\quad f(y,z)\epsilon^x(x,0,0) \\ \epsilon^{yz}(x,y,z) = &\quad \epsilon^{yz}(x,0,0) \end{aligned} \tag{2.46}$$

where the function $f(x,y)$ describes the modulation of the effective modal index across the system.

As in the surface mode matching technique, when Eqs. (2.46) are satisfied, the spatial mode profile of all TM waveguide modes again become independent of the the effective indices of refraction and do not couple to other modes. Fig. (2.13) shows an example of the anisotropic technique applied to the planar waveguide system.

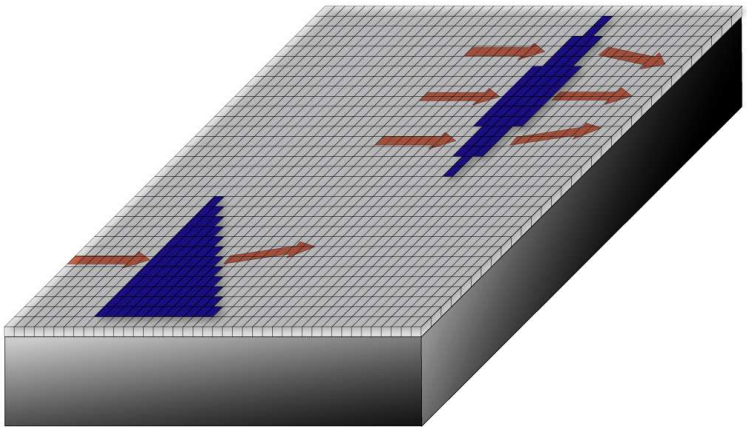

FIGURE 2.12: Rendering of an electroplasmonic system. The regions in blue can have the permittivity changed by applying an external electric field to create surface optic elements such as lenses and prisms. Arrows represent direction of surface waves.

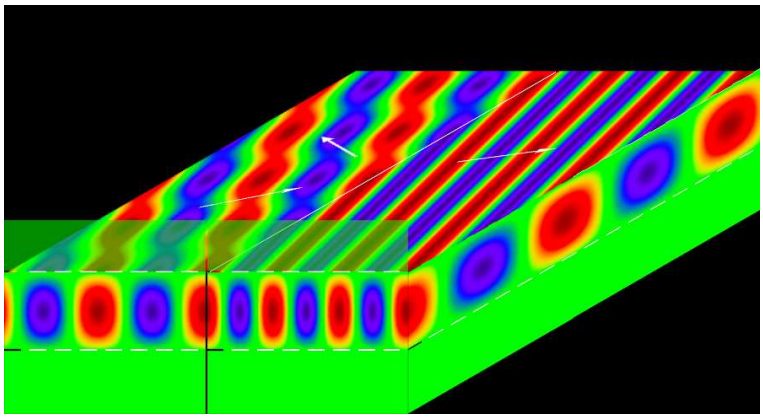

FIGURE 2.13: Simulation showing the mode matching via anisotropic metamaterials. Note how the index of refraction is changed and no extraneous modes are excited.

2.11 Conclusions

In this chapter a theoretical model was presented to minimize scattering of SPP energy from a change in index of refraction. The basis of this model lies in the use of anisotropic metamaterials to match the modal profile of the SPP wave on both side of an interface while still undergoing a change in the index of refraction. Because of the interdependence of the spatial profile κ on n_{eff} for isotropic materials, Eqs. (2.2 2.6), any change in one requires a change in the other. However, this work shows that with anisotropic materials, it is sufficient to keep the in-plane components of permittivity constant while the x-component is free to be changed, as long as the condition in Eq. (2.18) is satisfied. The anisotropic expression for n_{eff} was derived and it is shown that a change in ϵ^x enables a change in the index of refraction while ϵ^{yz} is still constant.

An approximate analytical approach to calculate the reflection and transmission coefficients for the anisotropic SPP supporting system is also derived in this chapter. It was shown that in the limit of weak scattering, this analytical approach matches that of the much more computationally intensive numerical results of COMSOL. A technique for approximating the inverse of a nearly diagonal matrix using a Taylor Series expansion was outlined and used in the derivation.

An application that will benefit from the scattering free 2D optics is that of electro-optics. It is possible to fabricate materials such that the permittivity can be altered by an applied electric field. By adjusting where the field is applied, it will be possible to manufacture optical elements such as lenses, prisms, and reflectors. The advantage to creating these elements by the use of electro-optics is that the elements can be *dynamically* created, destroyed, or otherwise altered. This will allow for an extremely fine-grained degree of control over surface waves.

The theory of utilizing anisotropic metamaterials to match the spatial profile of TM waves can be applied to other waveguide structures besides the surface wave presented for the bulk of this chapter. Anisotropic planar waveguides can also be designed to exhibit efficient light management.

3. PLASMONIC NANOLAYERED SYSTEMS

This chapter will describe the nanolayered structure and discuss methods for derivation of electromagnetic properties of such a structure.

3.1 Intro

Nanolayered composites are the basis for many new applications, including negative index systems, super- and hyperlenses, optical cloaks, and photonic funnels [6, 10, 21, 37, 44, 45, 46]. The layers of these structures are of only about $10 - 100$nm in size. Because this size is much smaller than the wavelength typically used (optical frequencies - $\sim 1\mu$), conventionally it has been assumed that a Effective Medium Theory (EMT) is sufficient to accurately describe the electromagnetic properties. However, in this chapter it will be shown through an exact calculation using the Transfer Matrix Method (TMM) that conventional EMT fails to account for non-local effects present if there is a large difference between permittivities. A derivation of an analytical approximation with a higher degree of accuracy is discussed.

There are many methods for fabrication of nanolayered materials, but the experiments that are discussed in this chapter were done with the use of electron beam evaporation (EBE) for the metallic layers, while the dielectric layers by plasma-enhanced chemical vapor deposition (PECVD). These fabrication techniques were briefly discussed in §1.1, but will be reviewed here. Electron beam evaporation consists of a target, in this case gold (Au), being subjected to an electron beam from a charged element under vacuum. The high energy electrons cause atoms of gold to be energized to a gaseous phase where they are allowed to precipitate to a thin solid layer coating the substrate material. By controlling the rate of the electron beam and the time, various layer thicknesses can be achieved.

The PECVD approach is similar to EBE, but instead of an electon beam, a chemical reaction is used to create the dielectric material vapor. In the case of PECVD, a plasma is used to assist the chemical process to allow for lower temperatures to be used. In the following experiments, a high index silicon was used for the substrate, gold (Au) for the metallic layers interspersed with

silica (SiO_2) layers for the dielectric.

3.1.1 Evolution of Plasmon modes in a Multi-layered System

An individual metal dielectric interface supports an SPP as described in §2.2. When two metal layers are brought brought to within a small distance of each other, the SPP modes on each surface interact with each other. This interaction leads to two combinations, an anti-symmetric and a symmetric SPP mode as illustrated in Fig. (3.1). As the gap distance between the metal layers is decreased, the splitting between the modal indices grows, in a similar manner to energy level splitting in quantum mechanics. Eventually as the gap distance is decreased further, the anti-symmetric mode experiences a cutoff, leaving only the symmetric mode known as a gap plasmon [47].

In a structure with three layers, a metal layer in between two dielectric layers, enclosed by two metal cladding regions, will in principle support four SPP combinations. However, if the metal film is within the cutoff range of the cladding layers. the total number of modes supported is two, the symmetric and anti-symmetric combinations of gap plasmons, shown in Fig. (3.2). Note that the modal indices continue to repulse from each other, yielding modes with effective indices much higher than that of an individual gap plasmon.

As additional metal strips are added to the above sandwich structure, the formation of additional supermodes is observed, one for each new metal-dielectric combination added. Thus, the total number of modes supported in the metal-dielectric nanolayered system with metallic claddings will be equal to the number of dielectric layers in the system.

An interesting case is when the standard condition for plasmon is reversed, ie. $|\epsilon_m| < \epsilon_d$. In this case, a single interface would not support an SPP, but the gap plasmon can exist. However, an antisymmetric gap plasmon exists with a *negative* refractive index [26] in the two-interface sytem in this case. In a way, the behavior of the metal-dielectric-metal system with $|\epsilon_m| < \epsilon_d$ is exactly opposite to that of $|\epsilon_m| > \epsilon_d$. The effective index of refraction is negative, and the cutoff of modes in one system is related to the appearance of modes in the other system (see Fig. (3.1)).

The traditional labeleing scheme used for modes in multilayer systems is based on the number of nodes in the field distributions. Accordingly, the mode supported at a single interface is labeled TM_0. The symmetric and anti-symmetric modes in the two inteface system are the TM_0

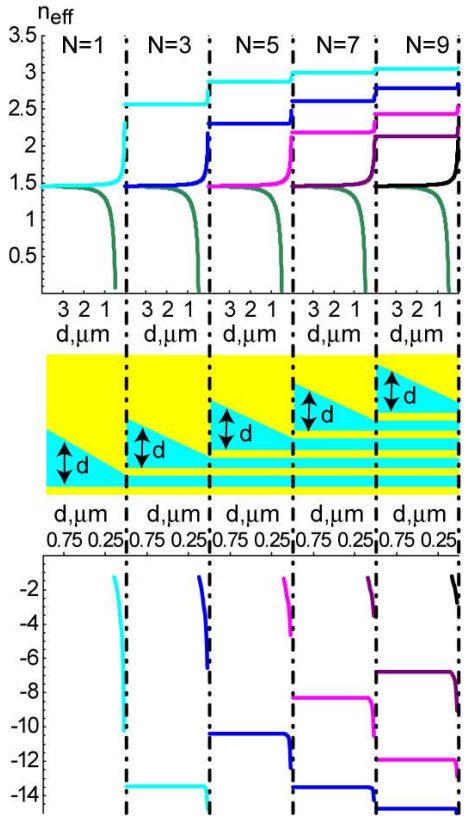

FIGURE 3.1: The evolution of coupled SPP modal indices in a layered material propagating in the z-direction. $n_{\text{eff}} = k_z c/\omega$ at $\lambda_0 = \omega/c = 1.55\mu m$ vs. the gap thickness is shown. As the gap is decreased, the SPP modal indices split into the anti-symmetric and symmetric modes with the anti-symmetric experiencing a cutoff and only the symmetric mode known as a gap plasmon survives. The top part of the figure corresponds to a positive index structure with $\epsilon_d = 1.444^2; \epsilon_m = -114.5 + 11.01i$ $(Au - SiO_2)$, while the bottom part is that of a negative index system with $\epsilon_d = 1.444^2; \epsilon_m = -1 + 0.1i$. The middle is a schematic showing the xz-crossection of the system.

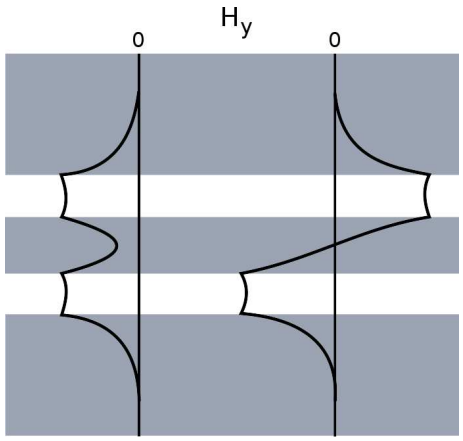

FIGURE 3.2: The field distributions (real part) of the symmetric (left) and anti-symmetric (right) gap plasmon modes. H_y is shown illustrating how the collective field decay profiles couple to create the gap plasmon.

and TM_1 modes, respectively. Unfortunately, the gap plasmon is also labeled as a TM_0 mode. Furthermore, if the cladding region is changed to a dielectric rather than a metal, the gap plasmon mode becomes a TM_2 mode.

To deal with this, we propose the use of a new classification scheme. The TM_0 and TM_1 modes are not confined to the bulk region and are known as long- and short-range plasmon polaritons [4, 48] and can extend into the dielectric cladding on a macroscopic scale. The other modes are highly confined to the bulk material and exhibit different properties, so it makes sense to call these modes bulk plasmon polaritons (BPPs). The first of these modes that exhibits a smooth profile will be designated BPP_0 and higher modes will be determined by their field profile, as illustrated in Fig. (3.3). In the traditional classification this would be a TM_2 mode because it has two nodes close to the cladding interface. Extending this scheme, it is seen that the BPP_n mode corresponds to what would be called TM_{n+2} in the traditional classification.

3.2 Structure

The schematic of the structure for the nanolayered structure is shown in Fig. 3.4. The *average* layer thicknesses a_1 and a_2 are in the range $10 - 100$ nm. The individual layers will have permittivities given by ϵ_1, ϵ_2. The propagation of the electromagnetic wave in this system

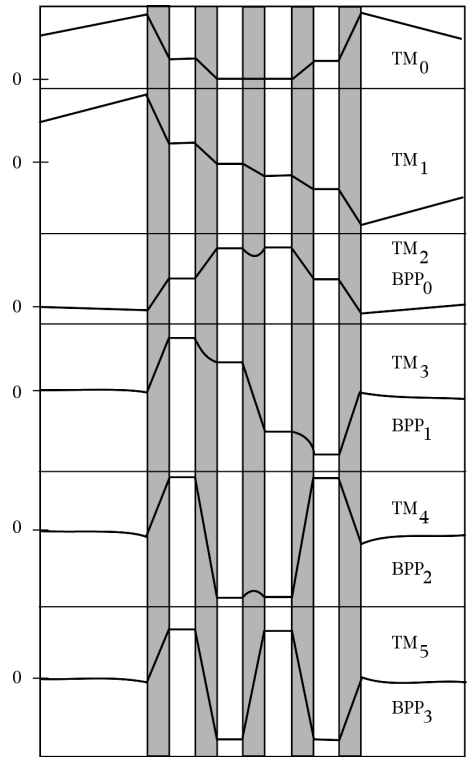

FIGURE 3.3: Six modes in a system with five metal layers, four dielectric layers, and dielectric cladding. The first two modes are the symmetric and anti-symmetric modes known as the long- and short-range plasmons. These modes penetrate the cladding on a macroscopic scale. The other modes are highly confined to the bulk structure and are designated the bulk plasmon polariton modes, BPP_n. Figure shows the strength of magnetic field versus coordinate across the structure.

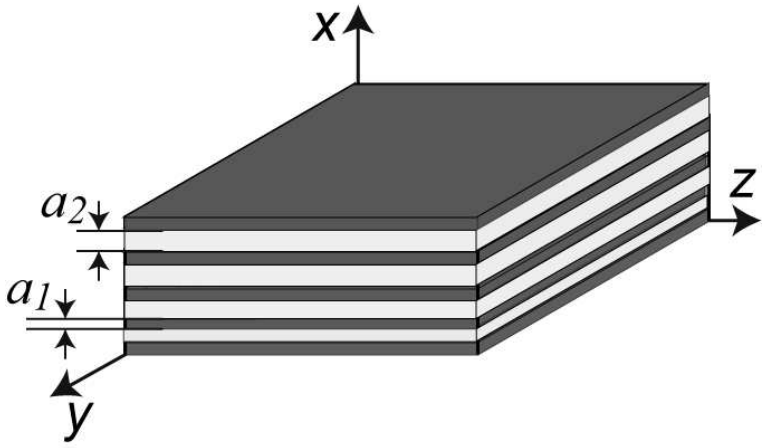

FIGURE 3.4: Schematic of the nanolayered structure. a_1 is the metal layer thickness and a_2 the dielectric thickness. Propagation of the bulk plasmon mode is in the $z-$ direction. Cladding layers are present on the top and bottom of the structure.

is described by Surface Plasmons, which were described in some detail in §2.2. As discussed previously, only TM polarizations are relevant in the description of SPPs, so TE polarizations will be only briefly mentioned in the following text.

The geometry is oriented so that the $x-$axis is oriented perpendicular to the plane defined by the layers, and since there is no difference between the y and z directions, the structure is oriented so that propagation will only take place in the $z-$direction. This allows for the simplification of $k_y = 0$.

3.3 Theory

In this section, several theories will be explored that describe the nano-layered structure. The simplest theory is the Effective Medium Theory. This was described as an overview in §1.1.1, but will be specifically implemented for the layered system in §3.3.1. Next, the exact but computationally expensive Transfer Matrix Method will be derived and discussed. Finally, an enhancement to the EMT will be introduced where non-local effects are taken into account. It will be shown in §3.4 that this enhancement to EMT will greatly increase the accuracy of results compared to the conventional EMT.

3.3.1 Effective Medium Theory: Applied to the Nano-layered system

Effective Medium theory assumes the characteristic size of the system is much smaller than the wavelength so that the electromagnetic radiation can be assumed to be a plane wave over the entire system.

Under the above condition, the elements of the permittivity tensor can be approximated as

$$\epsilon_{\alpha\beta} = \frac{\langle D_\alpha \rangle}{\langle E_\beta \rangle} \tag{3.1}$$

where α and β are coordinate directions. For the uniaxial nanolayer and other regular structures, off-diagonal elements of the permittivity tensor are 0, so the tensor reduces to

$$\hat{\epsilon} = \begin{pmatrix} \epsilon_x & 0 & 0 \\ 0 & \epsilon_{yz} & 0 \\ 0 & 0 & \epsilon_{yz} \end{pmatrix} \tag{3.2}$$

Thus, the problem of finding the *effective* permittivities is reduced to that of finding the average electric and displacement fields.

Using the geometry shown in Fig. (3.4), The average displacment and electric fields are given by

$$\begin{aligned} \langle D \rangle &= \frac{a_1}{a_1 + a_2} D_1 + \frac{a_2}{a_1 + a_2} D_2 \\ \langle E \rangle &= \frac{a_1}{a_1 + a_2} E_1 + \frac{a_2}{a_1 + a_2} E_2 \end{aligned} \tag{3.3}$$

where it is to be understood that the direction of the field is to be used to get the tensor elements. For ϵ_x, Eq. (3.1) can be solved by using the boundary condition that normal $\vec{D}$ must be continuous. This means that $D_1 = D_2 = D_x$, and the electric fields as $E_1 = \frac{D_x}{\epsilon_1}$ and $E_2 = \frac{D_x}{\epsilon_1}$. Then, ϵ_x simplifies to

$$\epsilon_x = \frac{\epsilon_1 \epsilon_2 \left(a_1 + a_2\right)}{\epsilon_1 a_2 + \epsilon_2 a_1} \tag{3.4}$$

Similarly, by using the boundary condition of continuous E_z, it is found that

$$\epsilon_z = \frac{a_1 \epsilon_1 + a_2 \epsilon_2}{a_1 + a_2} \tag{3.5}$$

These can also be rewritten in terms of the relative concentration $N = \frac{a_1}{a_1+a_2}$ as

$$\begin{aligned} \epsilon_x &= \frac{\epsilon_1\epsilon_2}{N\epsilon_2 + (1-N)\epsilon_1} \\ \epsilon_z &= N\epsilon_1 + (1-N)\epsilon_2 \end{aligned} \tag{3.6}$$

The important thing to note here is that only the relative concentration N and the permittivities of the two constituent materials is relevant to finding the effective permittivity. The advantage to this is that as long as the concentration is relatively constant in a metamaterial, the material can be random. However, as will be shown later, when the difference between the permittivities is large, a non-local effect due to the highly varying electric fields will cause this formula to not give accurate results.

3.3.2 Transfer Matrix Method

Maxwells Equations can be solved directly in the nano-layered case to yield a transfer matrix to find the dispersion relation.

To derive the following relations, it is convenient to be able to express the magnetic field in terms of the electric field. First, it is assumed that the propagating radiation is transverse magnetic (TM) so that the magnetic field has only a y component

$$\vec{H} = H_y = H_0 e^{ik_x x + ik_z z - i\omega t} \tag{3.7}$$

Then, use Ampere's Law

$$\vec{\nabla} \times \vec{H} = \frac{1}{c}\frac{\partial \vec{D}}{\partial t} \tag{3.8}$$

This yields

$$-ik_z H_y \hat{i} + iK_x H_y \hat{k} = \frac{1}{c}\frac{\partial \vec{D}}{\partial t} \tag{3.9}$$

Splitting $\vec{D}$ into components and performing the time derivative yields the two relationships

$$\begin{aligned} E_x &= \frac{k_z c}{\epsilon_x \omega} H_y \\ E_z &= -\frac{k_x c}{\epsilon_z \omega} H_y \end{aligned} \tag{3.10}$$

From these relations and the boundary conditions that tangential $\vec{E}$ and normal $\vec{D}$ are continuous, the following equations relating the amplitudes (a) of the fields in the j^{th} and $(j+1)^{th}$ layers can

be found

$$E_z^j = E_z^{j+1} \quad \Rightarrow \quad a_j^+ e^{ik_j x_j} + a_j^- e^{-ik_j x_j} - a_{j+1}^+ e^{ik_{j+1} x_j} - a_{j+1}^- e^{-ik_{j+1} x_j} = 0 \tag{3.11}$$
$$H_y^j = H_y^{j+1} \quad \Rightarrow \quad \frac{\epsilon_j^x a_j^+}{k_j} e^{ik_j x_j} - \frac{\epsilon_j^x a_j^-}{k_j} e^{-ik_j x_j} - \frac{\epsilon_{j+1}^x a_{j+1}^+}{k_{j+1}} e^{ik_{j+1} x_j} + \frac{\epsilon_{j+1}^x a_{j+1}^-}{k_{j+1}} e^{-ik_{j+1} x_j} = 0$$

where the $+, -$ indicates which direction the wave is propagating and all k's are assumed to be k_x values. Combining these equations to solve for a_{j+1}^+ and a_{j+1}^-,

$$\begin{aligned} a_{j+1}^+ &= \frac{1}{2} e^{-ik_{j+1} x_j} \frac{k_{j+1}}{\epsilon_{j+1}^x} \left[\left(\frac{\epsilon_{j+1}^x}{k_{j+1}} + \frac{\epsilon_j^x}{k_j} \right) a_j^+ e^{ik_j x_j} + \left(\frac{\epsilon_{j+1}^x}{k_{j+1}} - \frac{\epsilon_j^x}{k_j} \right) a_j^- e^{-ik_j x_j} \right] \\ a_{j+1}^- &= \frac{1}{2} e^{ik_{j+1} x_j} \frac{k_{j+1}}{\epsilon_{j+1}^x} \left[\left(\frac{\epsilon_{j+1}^x}{k_{j+1}} - \frac{\epsilon_j^x}{k_j} \right) a_j^+ e^{ik_j x_j} + \left(\frac{\epsilon_{j+1}^x}{k_{j+1}} + \frac{\epsilon_j^x}{k_j} \right) a_j^- e^{-ik_j x_j} \right] \end{aligned} \tag{3.12}$$

Putting these into a matrix form we get

$$\begin{bmatrix} a_{j+1}^- \\ a_{j+1}^+ \end{bmatrix} = \hat{T}_{j,j+1} \begin{bmatrix} a_j^- \\ a_j^+ \end{bmatrix} \tag{3.13}$$

where

$$\hat{T}_{j,j+1} = \frac{1}{2} \begin{bmatrix} (1+K)\, e^{i(k_{j+1}-k_j)x_j} & (1-K)\, e^{i(k_{j+1}+k_j)x_j} \\ (1-K)\, e^{-i(k_{j+1}+k_j)x_j} & (1+K)\, e^{-i(k_{j+1}-k_j)x_j} \end{bmatrix} \tag{3.14}$$

with $K = \frac{k_{j+1}\epsilon_j}{\epsilon_{j+1}k_j}$. A similar approach can be used for the case of TE waves yielding Eq. (3.14), but with $K = \frac{k_{j+1}}{k_j}$. This transfer matrix will allow us to calculate the amplitude coefficients for the $j+1$ layer knowing them for the j^{th} layer.

The real power of this formalism is that the transfer matrices can be multiplied together to obtain coefficients for the top layer relative to the bottom layer [49] as

$$\begin{bmatrix} a_N^- \\ a_N^+ \end{bmatrix} = \hat{T}_{N,N+1} \times \hat{T}_{N-1,N} \times \ldots \hat{T}_{2,3} \times \hat{T}_{1,2} \begin{bmatrix} a_0^- \\ a_0^+ \end{bmatrix} \tag{3.15}$$

where it is possible to calculate the amplitudes of the output from those at the incident side.

3.3.2.1 Photonic Crystals

An important application of these transfer matrices is that of the derivation of the photonic band equation also sometimes referred to as the photonic crystal equation. The layered photonic crystal is a structure as described in §3.2 but with the condition that it is exactly periodic in

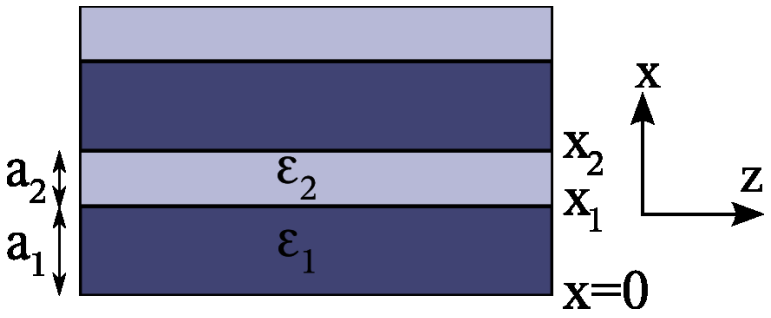

FIGURE 3.5: Schematic of the layered photonic crystal. The structure is periodic in ϵ with a periodic length $a_1 + a_2$.

$a_1 + a_2$ with respect to the permittivities, as illustrated in Fig. (3.5). From the Bloch theorem of periodicity, the periodic electric field can be described by

$$\vec{E}(a_1 + a_2) = e^{iq(a_1+a_2)}\vec{E}(0) \tag{3.16}$$

where q is the Bloch vector. In general the electric field in a given layer l is related to the backward and forward propagating waves

$$\vec{E}_l(x) = b_l^+ e^{ik_l^x x} + b_l^- e^{-ik_l^x x} \tag{3.17}$$

where the harmonic dependence has been left out. Using the transfer matrix method described earlier, the relationship between the amplitude coefficients is given by

$$\begin{bmatrix} b_3^- \\ b_3^+ \end{bmatrix} = \hat{T}_{23}\hat{T}_{12} \begin{bmatrix} b_1^- \\ b_1^+ \end{bmatrix} \tag{3.18}$$

Using Eq. (3.17)

$$E_3(a_1 + a_2) = b_3^- e^{-ik_3(a_1+a_2)} + b_3^+ e^{ik_3(a_1+a_2)} = \begin{bmatrix} 1 & 1 \end{bmatrix} \begin{bmatrix} e^{-ik_1(a_1+a_2)} & 0 \\ 0 & e^{ik_1(a_1+a_2)} \end{bmatrix} \begin{bmatrix} b_3^- \\ b_3^+ \end{bmatrix} \tag{3.19}$$

and

$$E_1(0) = b_1^- e^{-ik_1 0} + b_1^+ e^{ik_1 0} = \begin{bmatrix} 1 & 1 \end{bmatrix} \begin{bmatrix} b_1^- \\ b_1^+ \end{bmatrix} \tag{3.20}$$

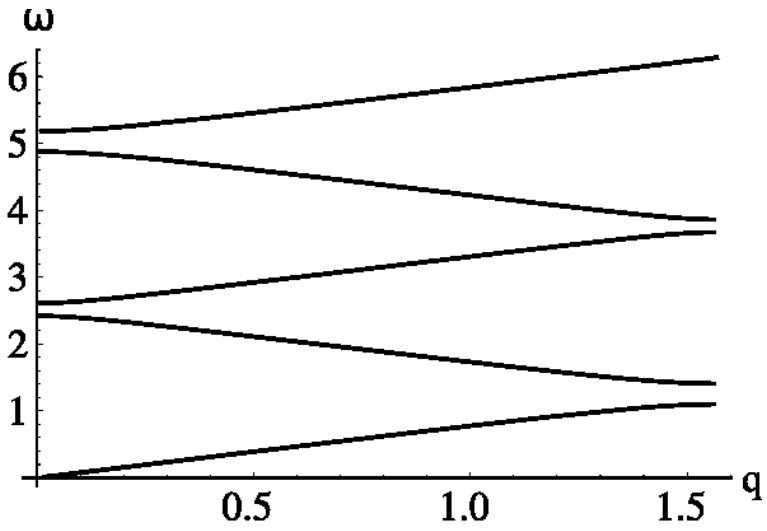

FIGURE 3.6: Band Structure plot of Eq. (3.24). Note the band gaps at some frequencies.

Putting these together with the Bloch equation (3.16),

$$\begin{bmatrix} 1 & 1 \end{bmatrix} \left[\begin{pmatrix} e^{-ik_1(a_1+a_2)} & 0 \\ 0 & e^{ik_1(a_1+a_2)} \end{pmatrix} \hat{T}_{23}\hat{T}_{12} - e^{iq(a_1+a_2)}\hat{I} \right] \begin{bmatrix} b_1^- \\ b_1^+ \end{bmatrix} = 0 \tag{3.21}$$

For this equation to have a non-trivial solution,

$$det\left[\hat{\Phi}\hat{T}_{23}\hat{T}_{12} - e^{iq(a_1+a_2)}\hat{I}\right] = 0 \tag{3.22}$$

where

$$\hat{\Phi} = \begin{bmatrix} e^{-ik_1(a_1+a_2)} & 0 \\ 0 & e^{ik_1(a_1+a_2)} \end{bmatrix} \tag{3.23}$$

Eq. (3.22) can be algebraically reduced to

$$\cos q(a_1 + a_2) = \cos k_1 a_1 \cos k_2 a_2 - \gamma \sin k_1 a_1 \sin k_2 a_2 \tag{3.24}$$

with $\gamma_{TM} = \frac{1}{2}\left(\frac{\epsilon_2 k_1}{\epsilon_1 k_2} + \frac{\epsilon_1 k_2}{\epsilon_2 k_1}\right)$ for TM polarization, and $\gamma_{TE} = \frac{1}{2}\left(\frac{k_1}{k_2} + \frac{k_2}{k_1}\right)$ for TE. The band structure of the photonic crystal structure can be seen in Fig. (3.6).

Photonic crystals can be used as low and high reflection coatings for lenses and mirrors. As seen in Fig. (3.6), band gaps exist at certain frequencies. The placement of these is affected by the size of the layers, the angle of incidence, and the permittivities of the layers. It is then

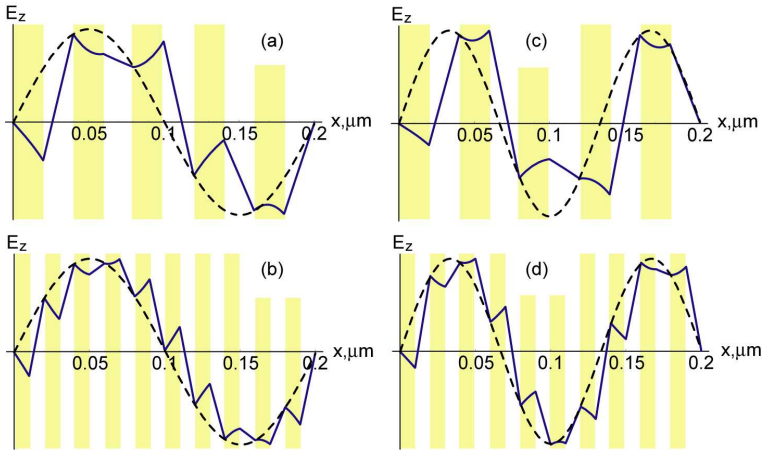

FIGURE 3.7: Field profile in nano-layered structure of alternating metal (white) and dielectric (yellow) layers with a metal cladding. Solid lines are transfer matrix method calculations while dashed are the effective medium theory for the TM_1 mode (a), (b), and the TM_2 mode (c), (d). (a) and (c) are for a system with total number of layers = 10. (b) and (d) for 20 layers.

possible to design a photonic crystal such that a desired ferquency is within the bandgap so that it is completely reflected, while other frequencies or other angles are allowed to pass through.

3.3.3 Non-local Effects

We define our system under investigation to be confined to be 200 nm thick with perfectly conducting metallic cladding layers where the layer thickness is then dependent upon how many layers are inside. For example, if there are 4 total layers inside the cladding region, each layer would be 50 nm thick.

Although the transfer matrix method does exactly solve the electrodynamics of the layered system, it is very computationally expensive to actually do the calculations. This is due to the large variation of the field on the scale of the structure, as seen in Fig. (3.7). Of note is how the field is highly oscillatory, especially in metal layers. This is due to the (usually) much larger in magnitude metallic permittivity relative to the dielectric permittivity, $|\epsilon_m| \gg \epsilon_d$.

Because of this oscillatory field profile, calculating via the transfer matrix method involves subtracting very large exponential terms to obtain relatively small field components. Due to the subtractive cancellation error introduced, terms must be calculated to much higher than machine precision. A standard **double** number usually has a precision of $15-16$ decimal places. However, the program Mathematica [50] has the ability to store numbers with arbritrary precision. As the

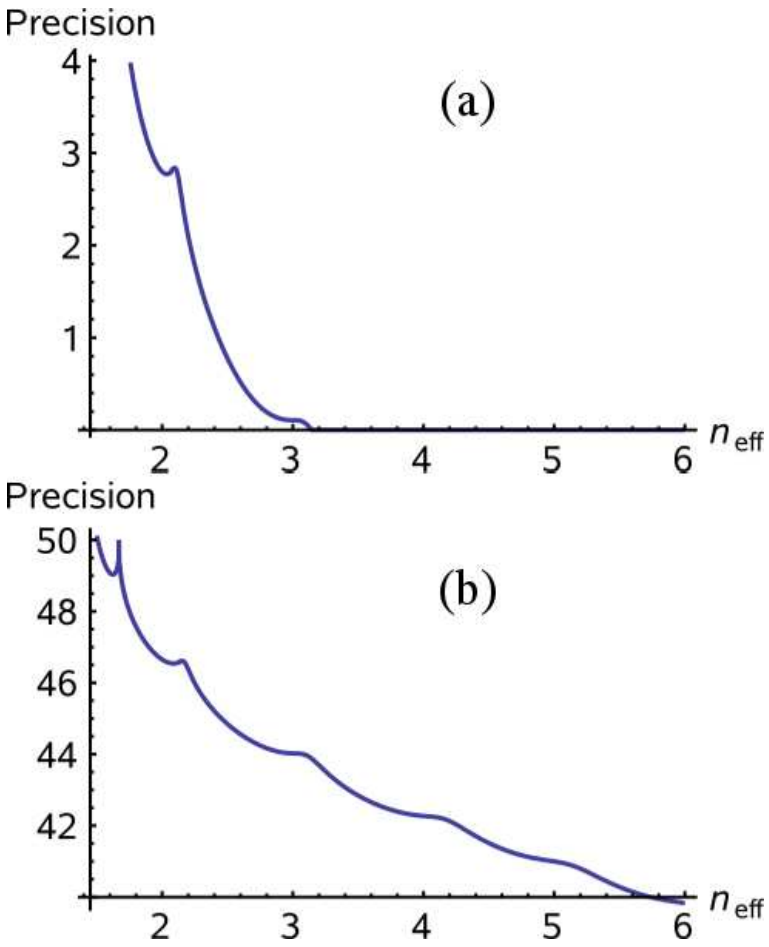

FIGURE 3.8: The effect of setting the precision on the result's precision. (a) Shows the very low precision in the result when the precision used is the machine precision ~ 16. (b) Much better results when the precision is set to 60.

number of layers is increased, so does the precision required to accurately store the information.

In the case of 20 layers, a precision of 60 places is required. Illustration of the effect the precision has on the results are shown in Figs.(3.8, 3.9). The nature of computers requires that increasing the precision past machine precision greatly increases the amount of memory and time required to do the computations. For example, to compute effective index of refraction values for a system with 20 layers, a current (2007) computer requires about 1 hour per value. To get the full picture, upwards of 50 values may be needed. Also, as the number of layers is increased, the time required to computation scales exponentially. To overcome this, an effective medium theory that gives accurate but much quicker results is desired.

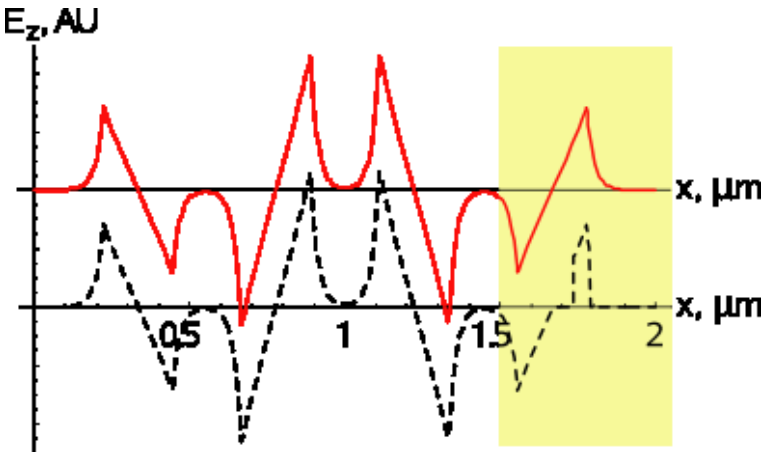

FIGURE 3.9: The effect of setting the precision on the field calculations. Note that in the shaded region how the lower precision calculates the field incorrectly.

The EMT is much faster in that it uses the same approach of the transfer matrix, but the EMT will produce effective permittivites such that the entire layered structure can be approximated to be a single *effective* medium. In other words, the effect of individual layers is averaged out so that the effective permittivies describe the properties of the system.

However, conventional EMT is unable to correctly produce results for systems with large variation of permittivity. To illustrate this, Fig. (3.10) shows the comparison of EMT and TMM for calculating the *effective* index of refration $n_{\text{eff}} = k_z c/\omega$ for each mode in the nanolayered structure. For these simulations, 100 ensembles were simulated with the relative concentration and total thickness fixed but random thicknesses for individual layers to simulate fabrication defects. The metallic permittivity used was $\epsilon_1 = -100$, roughly corresponding to Au, and dielectric permittivity $\epsilon_2 = 2$ for SiO_2. Variation was $\sim 10\%$ of average thickness. Clearly, the conventional EMT does not accurately calculate expected indices of refraction. The purpose of this section is to derive an extended EMT that does.

The dispersion relation for a TM wave propagating in an anisotropic material was derived in §2.3, Eq. (2.13)

$$\frac{\omega^2}{c^2} = \frac{k_x^2}{\epsilon_z^{eff}} + \frac{k_z^2}{\epsilon_x^{eff}} \tag{3.25}$$

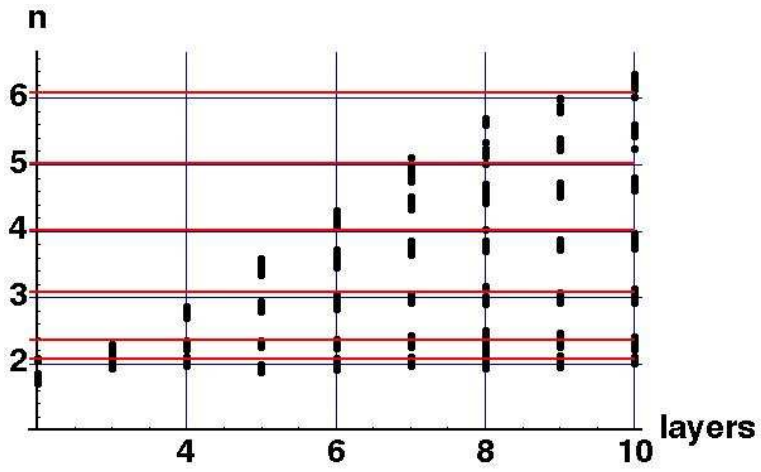

FIGURE 3.10: Comparison of conventional EMT and exact TMM calculations of effective modal index of refraction n vs. number of metal layers. EMT calculations are solid lines with dots for TMM. The first 6 modes (TM) are shown. Notice that EMT does not have any dependence on number of layers, only relative concentration of materials. EMT does give accurate results for lower order modes, but fails for higher order modes.

From §3.3.1 it was shown that the effective permittivities from conventional EMT are

$$\begin{aligned} \epsilon_x^{\text{eff}} = \epsilon_x^{(0)} &= \frac{\epsilon_1 \epsilon_2 \left(a_1 + a_2\right)}{\epsilon_1 a_2 + \epsilon_2 a_1} \\ \epsilon_z^{\text{eff}} = \epsilon_z^{(0)} &= \frac{a_1 \epsilon_1 + a_2 \epsilon_2}{a_1 + a_2} \end{aligned} \tag{3.26}$$

In the following derivation, corrections to these will be found so that

$$\begin{aligned} \epsilon_x^{\text{eff}} &= \frac{\epsilon_x^{(0)}}{1 - \delta_x(k,\omega)} \\ \epsilon_z^{\text{eff}} &= \frac{\epsilon_z^{(0)}}{1 - \delta_z(k,\omega)} \end{aligned} \tag{3.27}$$

To find these corrections, recognize that the system under discussion is very similar to a photonic crystal, assuming the individual layer thicknesses do not vary too much. So, use the photonic crystal equation dervied earlier in §3.3.2.1

$$\cos k_x(a_1 + a_2) = \cos k_1 a_1 \cos k_2 a_2 - \gamma \sin k_1 a_1 \sin k_2 a_2 \tag{3.28}$$

as a starting point. Assuming that $|k_1 a_1|, |k_2 a_2|, |k_x(a_1 + a_2)| \ll 1$, this equation can be expanded

by use of a Taylor series to 4^{th} order as

$$1-\frac{k_x^2(a_1+a_2)^2}{2}+\frac{k_x^4(a_1+a_2)^4}{24}=\left(1-\frac{k_1^2a_1^2}{2}+\frac{k_1^4a_1^4}{24}\right)\left(1-\frac{k_2^2a_2^2}{2}+\frac{k_2^4a_2^4}{24}\right)$$
$$-\frac{1}{2}\left(\frac{\epsilon_2k_1}{\epsilon_1k_2}+\frac{\epsilon_1k_2}{\epsilon_2k_1}\right)\left(a_1k_1-\frac{a_1^3k_1^3}{6}\right) \tag{3.29}$$

By putting this in the form of Eq. (3.27) we can find the corrections δ_x and δ_z. Note that if the 3^{rd} and higher order terms are disregarded in Eq. (3.29), the effective permittivities from conventional EMT will be recovered. Therefore it is surmised that the higher order terms are solely responsible for the corrections. After doing the algebra between Eqs. (3.25,3.27,3.29) together with the relation

$$k_{1,2}^2=\epsilon_{1,2}\frac{\omega^2}{c^2}-k_z^2 \tag{3.30}$$

the corrections are found to be

$$\begin{aligned}\delta_x &= \frac{a_1^2a_2^2\left(\epsilon_1-\epsilon_2\right)^2\epsilon_x^{(0)2}}{12\left(a_1+a_2\right)^2\epsilon_1^2\epsilon_2^2}\left(\epsilon_z^{(0)}\frac{\omega^2}{c^2}-\frac{k_x^2\left(\epsilon_1+\epsilon_2\right)^2}{\epsilon_z^{(0)}}\right) \\ \delta_z &= \frac{a_1^2a_2^2\left(\epsilon_1-\epsilon_2\right)^2}{12\left(a_1+a_2\right)^2\epsilon_z^{(0)}}\frac{\omega^2}{c^2}\end{aligned} \tag{3.31}$$

3.4 Results

To compare the non-local EMT to that of conventional EMT and also the exact TMM, simulations were done similar to those done to show how ineffective conventional EMT was in §3.3.3. Fig. (3.11) shows the improvement the non-local EMT has over the conventional theory. It is clearly seen that for lower order modes the theory much better matches the exact TMM values. The decrease in accuracy in the higher order modes can be explained by the fact that as the index of refraction is increased, so is the value of ka used in the Taylor series expansion for the derivation. This can be seen in that n_{eff} is proportional to k_z, which is related to k_x through the dispersion relation. It would seem intuitive that as k_z is increased, k_x should decrease, but the permittivity is negative, so an increase in k^z results in an increase in k_x. As ka increases, higher order terms are required in the expansion. Therefore, the non-local EMT can be extended further to account for the large n_{eff} modes by adding more terms to the expansion.

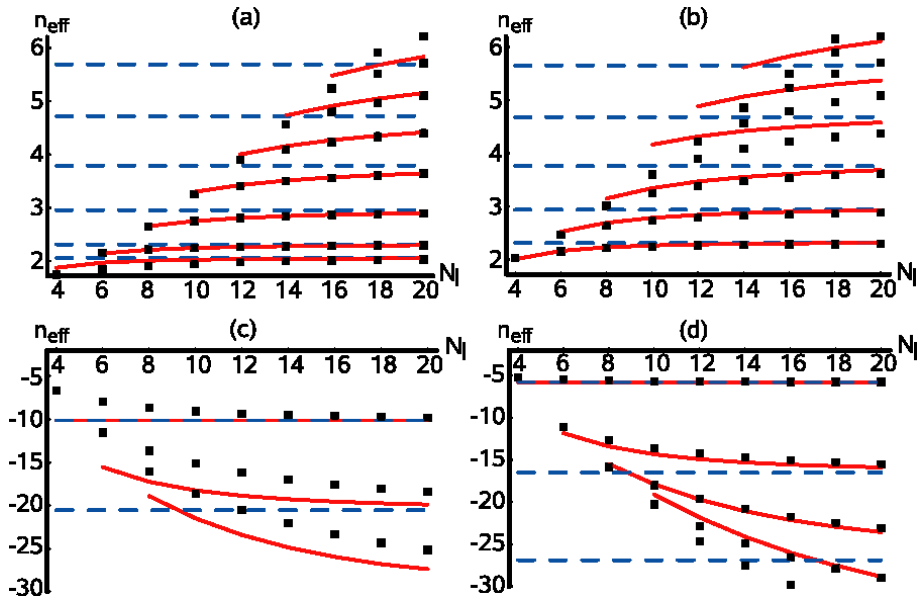

FIGURE 3.11: Comparison between effective modal indices of refraction of TM modes for a 200 nm thick planar waveguide. (a) and (c) are for a waveguide with perfectly conducting cladding walls. (b) and (d) with vacuum for the cladding. (a) and (b) are for a metamaterial with $\epsilon_1 = -114.5 + 11.01i; \epsilon_2 = 1.444^2$ (Au-SiO_2 composite). (c) and (d) are a negative refractive index material with $\epsilon_1 = -1 + 0.1i; \epsilon_2 = 1.444^2$. The wavelength used in all simulations was $\lambda_0 = 1.55\mu$m. Dots are the TMM calculations, dotted lines are the conventional EMT, while solid lines correspond to the non-local EMT derived in the text. N_l is the total number of layers.

Note that the standard condition for SPPs that $|\epsilon_1| > \epsilon_2$ where ϵ_1 is the permittivity of the metallic region is not the only possible solution. If one carefully observes the behavior under the condition that the reverse is true, a propagating mode is discovered with a negative index of refraction. This is shown in the lower figures of Fig. (3.11). However, for this condition to occur with relatively low dielectric permittivity, the modal indices $|n_{\text{eff}}|$ are very large and cause a much faster decrease in applicability of the non-local EMT.

When the total number of layers is large, the agreement with conventional EMT is seen. This is due to the fact that since the total thickness of the system is kept constant, increasing the number of layers results in a decrease in average layer thicknesses a_1,a_2. As this is decreased the lower order approximation becomes more valid since $|ka| \ll 1$.

To compare the non-local theory to real-world applications, an experimental group fabricated such a material for comparison. The material was made by alternating layers of silica (SiO_2) and gold (Au) on a silicon (Si) substrate. The Si substrate was half-cylinder in shape and was to be used as a high index prism to match the wavevector of the incoming laser light to that of the SPP. The SPP can be excited through a process known as either frustrated total internal reflectance or attenuated internal reflection. The idea of this process is as follows, the laser light is incident on the Si substrate and rotated through a series of angles, while always measuring the reflection intensity. The angle at which the reflectance drops to a minimum is the condition for most of the energy being transferred to the SPP. This is angle dependent because of trying to properly match the wavevector. Using the angle at which the reflection drops, it is possible to calculate the associated wavevector, and hence, the modal index. By making the prism to be a half-cylinder, a much larger range of angles could be used than allowed by the traditional triangular geometry of the Kretschmann and Otto configurations seen in Fig. (2.2).

Using the PECVD method described in the intro to this chapter, a layer of low index SiO_2 layer was deposited on the Si substrate. The layer thickness was measured to be roughly 25 nm. However, due to the very small size, the layer thickness could only be determined to 25 ± 5 nm. Similar issues arose when depositing the other layers of gold and the silica. The final structure was a total of six layers, three of dielectric alternating with three metallic.

Results from the experiment are shown in Fig. (3.12) where the first two bulk plasmon modes are clearly seen. The best theoretical fit corresponds to Si/(33nm silica)/(24 nm gold)/(24

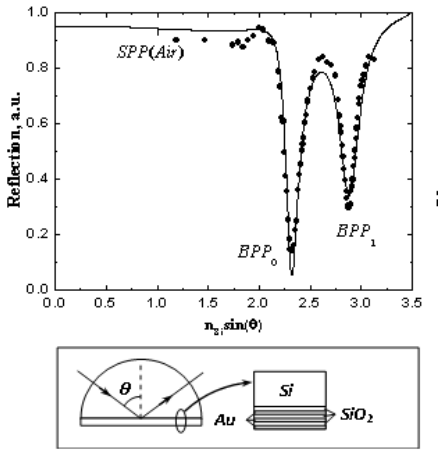

FIGURE 3.12: Results of the attenuated total reflection experiment on a layered structure with six layers of Au and SiO_2 on a Si substrate. Experimental data (dots) and theoretical fit (solid line) are shown indicating the BPP_0 and BPP_1 modes.

nm silica)/(26 nm gold)/(31 nm silica)/(24 nm gold) with average thicknesses being 29 for the silica layers and 25 for the gold, which is within the deposition target numbers.

3.5 Conclusions

In this chapter, three methods for calculating permittivities and electromagnetic fields for a nano-layered structure were shown. The Effective Medium Theory was derived for this example, and shown to be deficient for accounting for large variations in field due to large differences in constituent permittivities. For comparison purposes, the Transfer Matrix Method was also derived. In principle the Transfer Matrix Method is exact, but computationally expensive to use for a large number of layers. To overcome this problem, a Non-local effective medium theory was derived by assuming the layered structure is similar to a photonic crystal. It was shown that although still not as accurate as the transfer matrix, the extended effective medium theory greatly outperforms that of the conventional effective medium theory, while having comparable computation times. It was shown that the non-local EMT can accurately describe a real-world experimental version of the nano-layered system made of a gold-silica composite.

It was also shown that the layered system can support high-index modes that are confined

to spatial areas as small as $\lambda/8$ This confinement can be used in applications such as nano-guiding of light like photonic funnels [45]. Being able to confine light to such a scale is important for waveguide-optical fiber coupling.

4. PLASMONIC NANOWIRE SYSTEMS

4.1 Introduction

As discussed in previous chapters, anisotropic dielectric permittivity has uses in several areas of optics, including sensors, spectroscopy, and microscopy [51, 52, 53, 54, 55]. It can also be utilized to realize non-magnetic, non-resonant negative index of refraction materials [21, 37] as discussed in §1.2.2. This chapter will derive a Generalized Maxwell Garnett (GMG) theory that takes into account the shape and distribution of the wires. This is in contrast to the conventional Effective Medium Theory where the only parameter used in calculating the effective permittivity is the relative concentration.

In naturally occuring materials the maximum relative difference of dielectric permittivity (figure of merit), FOM $= \frac{\epsilon_{xy}-\epsilon_z}{\text{Max}(\epsilon)}$ is only about 30%. We will show in this chapter how a nanowire based system can be designed to have a FOM $> 100\%$, similar to what was possible with the nanolayered structures in the previous chapter. We further show how as little as 10% stretching/compression of the nanowire structure can achieve this.

We will also use 3D numerical simulations to verify the accuracy of the GMG as an approximation technique.

4.2 Structure

As discussed in §1.1, metamaterials are man made structures defined by subwavelength features. The nanowire metamaterial structure is made up of a system of metallic nanowires on the order of less than 100 nanometers in diameter, embedded in a dielectric host. Figure 4.1 is a representation of such a system.

The nanowires with permittivity ϵ^{in} are embedded into a host material with ϵ^{out}. The nanowires are assumed to be parallel and define the optic axis of the material. This direction will be defined to be the z-direction. To develop a general theory the nanowires are assumed to have elliptical crossections with semiaxes r_x and r_y. We also assume the entire structure can be

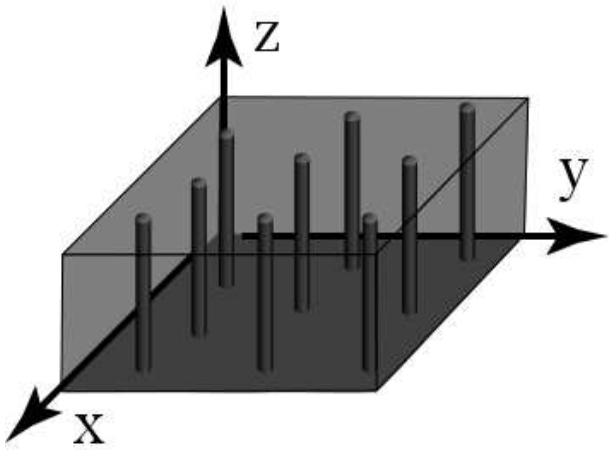

FIGURE 4.1: Schematic of Nanowire structure

stretched/compressed so that the wires can be anisotropically distributed. The distance between nearest neighbor nanowires is defined to be l_x and l_y.

4.3 Theory

4.3.1 Analytical Approximation

To develop an effective medium theory , the metamaterial is assumed to be homogeneous where $r_\alpha, l_\alpha \ll \lambda_0$, and the relative concentration of wire to host is small $N \ll 1$. In addition, if the wire material is metallic ($\epsilon^{\text{in}} < 0$), the requirement that $r_\alpha \leq \sigma$, with σ being the skin depth, must also be fulfilled. Under these conditions, Maxwell's equations, Eq. (1.9), have solutions represented as a series of plane electromagnetic waves inside a material with an effective dielectric permittivity given by

$$\epsilon^{\text{eff}}_{\alpha\beta} = \frac{\langle D_\alpha \rangle}{\langle E_\beta \rangle} \tag{4.1}$$

where α, β correspond to cartesian coordinates x, y, z, and the brackets correspond to average displacement and electric fields, respectively. If the permittivity inside the wire, ϵ^{in}, and outside the wire, ϵ^{out} are isotropic, this effective permittivity tensor becomes diagonal $\epsilon^{\text{eff}}_{\alpha\beta} = \delta_{\alpha\beta}\epsilon^{\text{eff}}_{\beta\beta}$ where $\delta_{\alpha\beta}$ is the Kronecker delta. By using the boundary condition that E_z must be continuous along

the surface of the wire (z-direction), ϵ_z^{eff} can be found by

$$\begin{aligned} \langle D_z \rangle = N D^{\text{in}} + (1-N)\, D^{\text{out}} = &\quad N\epsilon^{\text{in}} E^0 + (1-N)\,\epsilon^{\text{out}} E^0 \\ \langle E_z \rangle = &\quad N E^0 + (1-N)\, E^0 \\ \Rightarrow \epsilon_z^{\text{eff}} = &\quad N\epsilon^{\text{in}} + (1-N)\,\epsilon^{\text{out}} \end{aligned} \tag{4.2}$$

Finding ϵ_x^{eff} and ϵ_y^{eff} can not be done directly as the relationship between the electric fields is yet to be derived.

$$\begin{aligned} \langle D_\alpha \rangle = &\quad N D_\alpha^{\text{in}} + (1-N)\, D_\alpha^{\text{out}} \\ \langle E_\alpha \rangle = &\quad N E_\alpha^{\text{in}} + (1-N)\, E_\alpha^{\text{out}} \\ \epsilon_\alpha^{eff} = &\quad \tfrac{N\epsilon^{in} E_\alpha^{in} + (1-N)\epsilon^{out} E_\alpha^{out}}{N E_\alpha^{in} + (1-N) E_\alpha^{out}} \end{aligned} \tag{4.3}$$

The problem is now reduced to finding the relationship between E^{out} and E^{in} to the external field E^0 such that 4.3 can be simplified to parameters that are known, such as permittivities of the wires and the dielectric host, and geometrical factors such as separation of wires, etc... It should be noted that for isotropic geometries, $E^{\text{out}} = E_0$ because the excitation fields cancel, and the problem reduces to that developed in conventional EMT. However, for a more *Generalized* Maxwell Garnett (GMG) theory, we must consider anisotropic geometries as well. In these anisotropic cases, a feedback field scattered from all the other nanowires is excited given by χE^0. This excitation field in turn excites another field given by $\hat{\chi}^2 E^0$, which excites another field and so on ad infinitum. This can be expressed as $E^0 + \sum_j \hat{\chi}^j E^0$, which can be rewritten as $\left(\delta_{\alpha\beta} - \chi_{\alpha\beta}\right)^{-1} E_\beta^0$. According to Ref. [19], this feedback tensor becomes diagonal for rectangular, triangular, and other highly symmetric lattices, and even some random nanowire nanowire arrangements, leading to the expression $(1 - \chi_{\alpha\alpha})\, E_\alpha^0$.

We will show a derivation for χ for the simplified case of $r_x = r_y$, so the wires have a circular cross section, but the distance between wires is anisotropic.

Since we have assumed the field to be homogeneous inside the wire, it can be expressed as [56]

$$E_{x,y}^{\text{in}} = \frac{\epsilon^{\text{out}}}{(1-n_{x,y})\epsilon^{\text{out}} + n_{x,y}\epsilon^{\text{in}}} E^{\text{out}} \tag{4.4}$$

where $n_x, n_y = r_y/(r_x + r_y), r_x/r_x + r_y)$ are depolarization factors [57, 56]. Note that in the case of $r_x = r_y, n_{x,y} = 1/2$ so Eq. (4.4) reduces to

$$E^{\text{in}} = \frac{2\epsilon^{\text{out}}}{\epsilon^{\text{out}} + \epsilon^{\text{in}}} E^{\text{out}} \tag{4.5}$$

The dipole moment of this system is then

$$P = \frac{\pi r_x r_y}{4\pi} \frac{\epsilon^{\text{in}} - \epsilon^{\text{out}}}{(1-N)\,\epsilon^{\text{out}} + N\epsilon^{\text{in}}} \tag{4.6}$$

with $\pi r_x r_y$ begin the crossectional area of the wire. The electric field at the origin excited by all dipoles (see Jackson [19], Sec. 4.5) is then

$$\begin{aligned} E_x &= \tfrac{P}{A^2} \textstyle\sum_{i,j} \frac{l_x^2 i^2 - l_y^2 j^2}{\left(l_x^2 i^2 + l_y^2 j^2\right)^2} \\ &= \tfrac{P}{A^2} \left[\tfrac{1}{l_x^2} \textstyle\sum_{i,j} \frac{i^2}{\left(i^2 + \frac{l_y}{l_x}^2 j^2\right)^2} - \tfrac{1}{l_y^2} \textstyle\sum_{i,j} \frac{j^2}{\left(j^2 + \frac{l_x}{l_y}^2 i^2\right)^2} \right] \end{aligned} \tag{4.7}$$

where $A = l_x l_y$, and i, j determines the coordinates of each wire. Eq. (4.7) can be expressed as

$$E_x = \frac{P}{A^2 l_x l_y} \left[\alpha S(\alpha) - \frac{1}{\alpha} S(\frac{1}{\alpha}) \right] \tag{4.8}$$

where $\alpha = l_y/l_x$ and $S(\alpha) = \sum_{i,j} \frac{i^2}{(i^2+\alpha^2 j^2)^2}$. Note that while $S(\alpha) = \infty; \alpha S(\alpha) - \frac{1}{\alpha} S(\frac{1}{\alpha})$ is finite.

To simplify the function $S(\alpha)$, note that since i and j are being summed from $-\infty$ to ∞ but are always squared, this can be reduced to

$$S(\alpha) = 4 \sum_{i=1}^{\infty} \sum_{j=1}^{\infty} \frac{i^2}{\left(i^2 + \alpha^2 j^2\right)^2} + 2 \sum_{i=1}^{\infty} \frac{1}{i^2} \tag{4.9}$$

as illustrated in Fig. (4.2).

By use of Mathematica [50], the first sum in Eq. (4.9)

$$\sum_{i=1}^{\infty} \frac{i^2}{(i^2 + \alpha^2 j^2)^2} = \frac{\pi \coth(\alpha j \pi) - \alpha j \pi \operatorname{csch}^2(\alpha j \pi)}{\alpha j} \tag{4.10}$$

and the second sum is $\frac{\pi^2}{3}$, from Gradshteyn and Ryzhik [58] Eq. (0.223 3). Eq. (4.10) can be further reduced such that

$$S(\alpha) = \frac{\pi}{\alpha} \sum_{j=1} \frac{d}{dj} \left[j \coth(\alpha j \pi) \right] + \frac{\pi^2}{3} \tag{4.11}$$

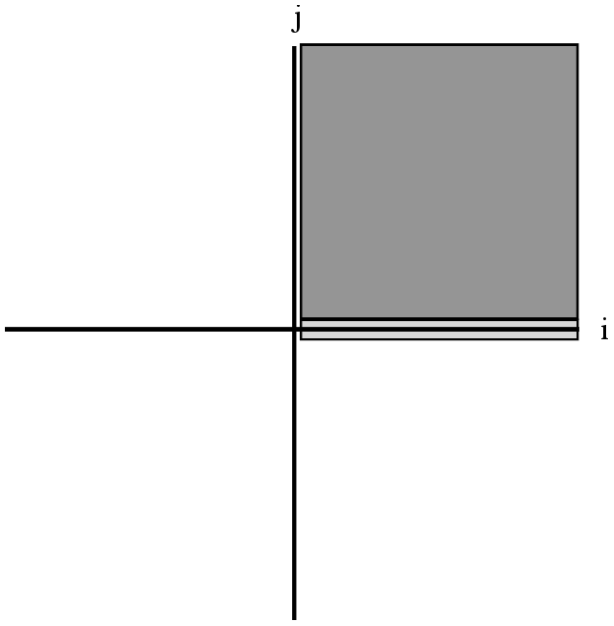

FIGURE 4.2: Shows how the sums in the function $S(\alpha)$ can be reduced. Instead of summing over all four quadrants, only sum over all values in the first quadrant for $j \geq 1$ (darker shaded region) and multiply by 4, plus the terms where $j = 0$ is equivalent to summing over the twice the x-axis (lighter shaded region).

Assume that $\alpha \approx 1 + \delta$ where $\delta \ll 1$ and numerically calculating the sum results in

$$\chi_\alpha = \frac{1}{4Al_xl_y} \frac{\epsilon^{\text{in}} - \epsilon^{\text{out}}}{(1-N)\,\epsilon^{\text{out}} + N\epsilon^{\text{in}}} 7.22\Delta_\alpha \tag{4.12}$$

where $\Delta_x, \Delta_y = l_x/l_y - 1, l_y/l_x - 1$ is the lattice distortion vector.

The more general case of elliptical crossection of wires can be derived in a similar method, and results in

$$\chi_\alpha = -0.16N\Delta_\alpha P_\alpha \left(\epsilon^{\text{in}} - \epsilon^{\text{out}}\right) \tag{4.13}$$

with $P_\alpha = a/\left[\epsilon^{\text{out}} + n_\alpha \left(\epsilon^{\text{in}} - \epsilon^{\text{out}}\right)\right]$. Note that in both Eqs. (4.12,4.13), if $l_x = l_y$, $\chi_\alpha = 0$, corresponding to the well known conventional Maxwell-Garnett result.

This interaction between wires changes the "microscopic" field that is acting on each wire, therefore both the field inside the wire

$$E_\alpha^{\text{in}} = \frac{\epsilon^{\text{out}} P_\alpha}{1 - \chi_\alpha} E_\alpha^0 \tag{4.14}$$

and the average field in between the wires from the dipoles

$$E_\alpha^{\text{out}} = \left[1 + \frac{NP_\alpha(\epsilon^{\text{in}} - \epsilon^{\text{out}})\left(Q(N)\left(\Omega_\alpha + \Delta_\alpha\right) - \pi\Omega_\alpha\right)}{2\pi\left(1-N\right)\left(1-\chi_\alpha\right)}\right] E_\alpha^0 \tag{4.15}$$

with $Q(N) = \pi - 1 - N(\pi - 2)$ and shape vector $\Omega_x, \Omega_y = r_x/r_y - 1, r_y/r_x - 1$. Now, Eqs. (4.13, 4.14, 4.15) can be used to calculate the effective permittivity given by Eq. (4.3)

$$\epsilon_\alpha^{\text{eff}} = \frac{N\epsilon^{\text{in}}E_\alpha^{\text{in}} + (1-N)\,\epsilon^{\text{out}}E_\alpha^{\text{out}}}{NE_\alpha^{\text{in}} + (1-N)\,E_\alpha^{\text{out}}}$$

4.4 Numercial Results

The system can be numercially solved by using the Discrete Dipole Approximation (DDA) [59], also known as the Coupled Dipole Approximation. DDA assumes that the system under study is a continuum of polarizable points that have a dipole moment in response to a local electric field. There is an available program that can calculate this called DDSCAT [60] written in Fortran. The program can calculate scattering and absorption of light from irregular particles.

We decided to create our own code that did a similar calculation (source code in Appendix A). This code was also written in Fortran and would approximate a given geometry as a system of particles that are polarizable and so have a dipole moment when exposed to an external electric field. The program uses the coupled dipole equations for 2-D

$$\vec{d}_i = \alpha\left(\vec{E}_{ext} + \sum_{i\neq j}\hat{G}_{ij}\vec{d}_j\right) \tag{4.16}$$

where $\alpha \approx \frac{0.57^2}{2}\frac{\epsilon-1}{\epsilon+1}$ and $\hat{G}_{\alpha\beta} = -\frac{2\delta_{\alpha\beta}}{R^2} + \frac{4r_\alpha r_\beta}{R^4}$ is the dyadic Green's function for point dipoles in 2-D. This is valid in the limit where the wavelength is much larger than the characteristic size of the system so that the light can be approximated as a plane wave.

We found that approximating the nanowires as simple, single dipoles did not yield accurate results, so instead a system was devised where each nanowire comprised of several smaller slightly overlapping dipole sources. This is illustrated in Figure 4.3.

Eq 4.16 can be solved for the dipole moment $\vec{d}$, which in turn is related to $\mathbf{P}$, the dipole moment per unit volume. This in turn can be substituted in Eq 1.4 to find χ_e, which, using 1.6 gives ϵ.

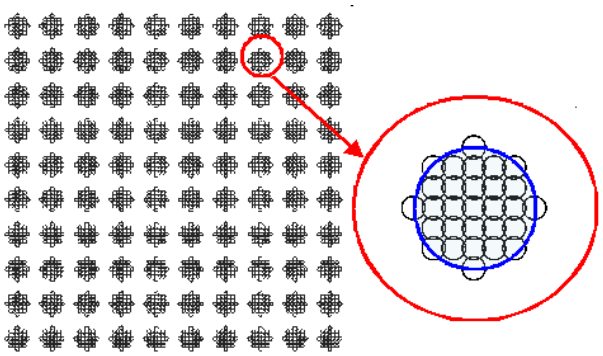

FIGURE 4.3: Schematic of approximation of dipoles used in Coupled Dipole Equation program. Inset is a close-up where the circle represents the "real" nanowire being simulated by smaller wires

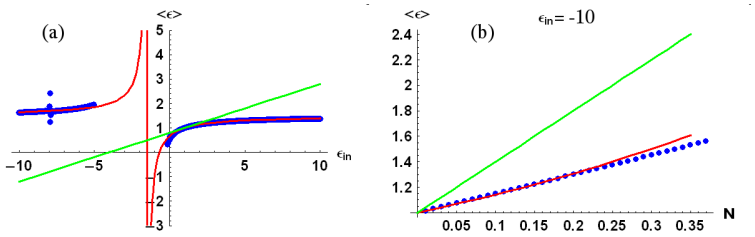

FIGURE 4.4: Numerical simulations vs. Effective Medium theory for the case of isotropically distributed wires. Dots are numerical values from DDA simulations as described in the text. Lines are EMT calculations for ϵ_{xy} (Red) and ϵ_z (Green). (a) is where the permittivity of the metal wire inclusions is varied. (b) shows the effect of relative concentration when $\epsilon_{\text{in}} = -10$. Note that as the concentration is increased, the approximation for EMT is no longer valid.

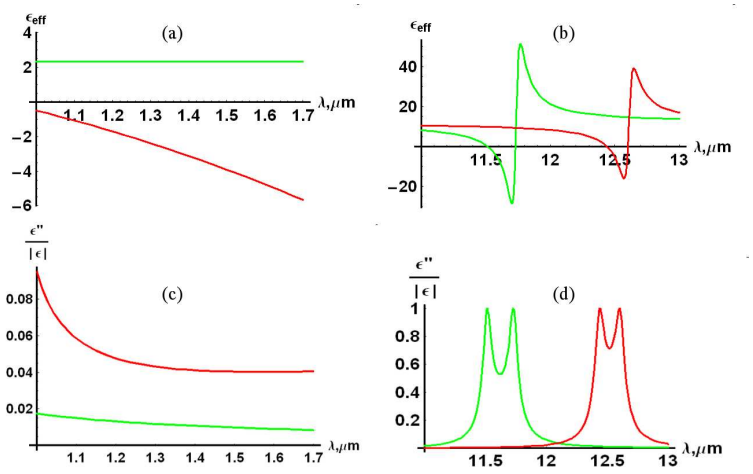

FIGURE 4.5: Real (a), (b) and imaginary (c),(d) components of the permittivity tensor for a wire composite of Ag-SiO_2 (a),(c) and SiC-Si (b),(d). Red lines are ϵ_{xy} and Green show ϵ_z as a function of wavelength. The Ag-SiO_2 has a concentration $N = 0.05$, $N = 0.1$ for the SiC-Si structure. Note the relatively small absorption in the negative refractive index region for Ag-SiO_2.

Fig. (4.4) shows the excellent agreement with EMT and numerical simulations for the case of isotropically distributed wires. Of note in this case is that when $\epsilon_{\text{in}} < -5$, the FOM described in §4.1 is greater than 100%. In other words, the effective permittivities in the permittivity tensor $\hat{\epsilon}$ have different sign, which is a condition required for some applications such as non-magnetic negative refractive index materials [21], also described in some detail in §1.2.2. Other applications that would benefit from this extreme anisotropy would be high-performance polarizers [55] and subwavelength light guiding [53, 45, 46].

We applied our EMT also to an isotropically distributed wire system composed of realistic materials. The results of these are shown in Fig. (4.5). We show that for telecom wavelength ($1.55\mu m$), the silver-silica wired structure, even at a low concentration of $N = 0.05$, shows promise as a low-loss NIM with the fabricationally easier isotropic arrangement.

To numerically simulate the anisotropically distributed wire arrangement, the finite element program COMSOL [43] was used. The advantage of this program is that it is commercially available and can simplify the simulation by using periodic boundary conditions. The idea is as follows, a single nanowire is drawn inside of a rectangular region defined by the lengths l_x, l_y and the boundary conditions for the fields are entered. The nanowire can be made to have an arbitrary shape, but as our theory is limited to ellipsoidal shapes, this limitation was also implemented in

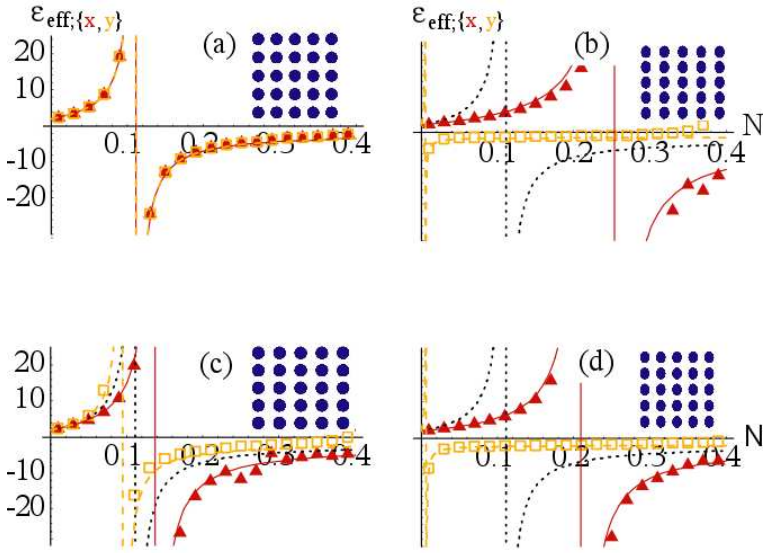

FIGURE 4.6: Effect of anisotropically distributing nanowires and wire shape. Material parameters used were $\epsilon^{\text{in}} = -2.5, \epsilon^{\text{out}} = 2$ corresponding to Ag nanowires in a ploymer with a vacumn wavelength of $\lambda_0 = 360$ nm. Red triangles (COMSOL) and solid lines (EMT) show ϵ_x while orange squares and dashed lines show ϵ_y. (a) Isotropic system with $\Delta_x = \Omega_x = 0$. Note there is no difference between x- and y-direction in this case. (b) $\Delta_x = 0.2, \Omega_x = -0.2$ (c) $\Delta_x = 0.2, \Omega_x = 0$ (d) $\Delta_x = 0, \Omega_x = -0.2$. Note that in the anisotropic systems that ϵ_x and ϵ_y have opposite in sign permittivity for some range of the concentration N. Insets show a crossection of the wires in each case.

the simulations. One advantage that the program COMSOL has is that once the initial problem is designed, the program can output a script file that can be easily modified to loop through various changes to be studied. For example, to study the effect stretching would have on the system, design the system in the graphical mode of COMSOL, output the file to a "script" file, and implement a loop that will change the value of the length scale in one direction, say l_y. The program can then calculate the dependent properties such as the relative concentration and the effective permittivities in each direction (source code in Appendix B).

The excellent agreement between the numerical simulations done with COMSOL and the generalized Maxwell-Garnett theory are shown in Fig. (4.6). Of particular note is that it is possible to control the effective permittivity in all three directions via concentration, distance between wires, and wire shape. By suitable choice of constituent materials it is possible to achieve nearly any desired combination of $\epsilon_x, \epsilon_y, \epsilon_z$. The effect of absorption in the system is shown in Fig. (4.7).

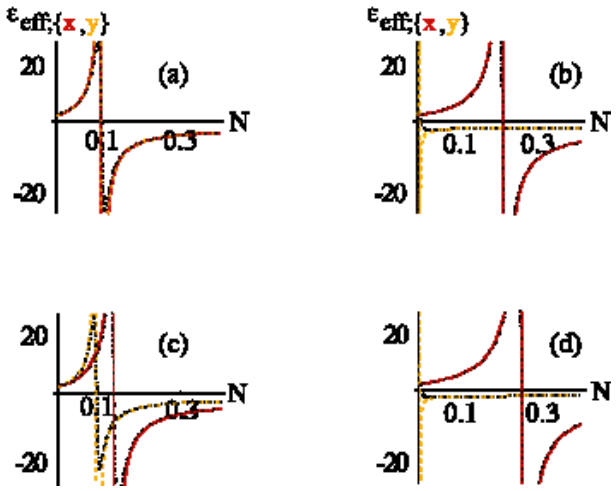

FIGURE 4.7: The effect of adding absorption to the system in Fig. (4.6) by making $\epsilon^{\text{in}} = -2.5 + 0.04i$.

It was pointed out in Refs. [61, 62, 63, 64] that the individual components of $\hat{\epsilon}$ may be strongly affected by spatial dispersion. To explore these effects we used COMSOL to identify the eigenwaves propagating in the x-direction through a planar waveguide with the nanowire core consisting of Ag wires in a Si host with a relative concentration of 10%. The waveguide has a thickness of d in the z-direction and the waveguide walls are assumed to be perfectly conducting. In this case, $k_y = 0, k_z = \pi/d$ and the dispersion relation is given by Eqs. (2.12, 2.13)

$$\begin{aligned} \frac{\pi^2}{\epsilon_y^{\text{eff}} d^2} + \frac{{k_x^{(TE)}}^2}{\epsilon_y^{\text{eff}}} &= \frac{\omega^2}{c^2} \\ \frac{\pi^2}{\epsilon_x^{\text{eff}} d^2} + \frac{{k_x^{(TM)}}^2}{\epsilon_z^{\text{eff}}} &= \frac{\omega^2}{c^2} \end{aligned} \tag{4.17}$$

where $\omega = 2\pi/\lambda_0$, k_x is the modal wavevector, c the speed of light, and d the waveguide thickness. Again, excellent agreement between the analytical expressions and numerical results in Fig. (4.8).

4.5 Conclusions

In this chapter we have described an anisotropic metamaterial based on a plasmonic nanowire strucutre. We derived a generalized approach to conventional Maxwell-Garnett theory that adds inclusion shape and arrangement as additional parameters to the relative concentration in finding

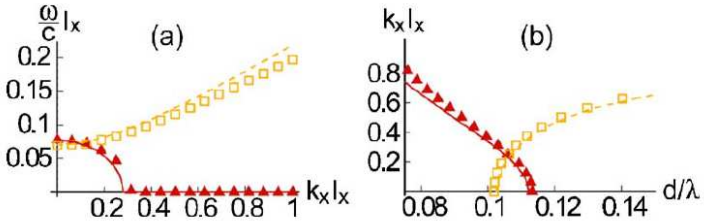

FIGURE 4.8: (a) Dispersion of the TM_0 (red triangles, solid lines) and TE_0 (orange squares, dashed lines) modes in a nanowire based waveguide with thickness $d = 400$ nm. Material parameters were $\epsilon^{\text{in}} = 13, \epsilon^{\text{out}} = -120, \Delta_x = 0.2, \Sigma_x = -0.2, l_x = 40\text{nm}, r_x = 10\text{nm}$. Note the negative refractive index TM mode. (b) Modal propagation constant $k_x l_x$ for $\lambda = 1.5\mu$m as a function of d. The generalized effective medium theory breaks down as $|k_\alpha l_\alpha| \to 1$.

an effective permittivity for the nanowire metamaterial. We also described a numerical approach to solving for $\hat{\epsilon}$ via a Coupled Dipole Approach. Eventually we settled on using the commercial program COMSOL to numerically simulate for the case of anisotropic distribution of wires and non-circular wire shape.

We showed the excellent agreement between the numerical simulations and GMG and the degree of control of effective permittivities achievable with stretching/compression of the structure. Several applications exist to take advantage of the degree of control afforded via the anisotropic nanowire based metamaterials, including negative index of refraction and high-performance polarizers.

5. CONCLUSIONS AND OUTLOOK

In the first chapter we introduced the theme of this thesis, that of anisotropic plasmonic structures. Background material of the physics behind effective medium theories, dielectric anisotropy, and negative index of refraction materials, including a method to achieve left-handedness via anisotropic metamaterials was shown.

The second chapter introduces a theoretical model to minimize scattering of SPP energy from a change in index of refraction. The basis of this model lies in the use of anisotropic metamaterials to match the modal profile of the SPP wave on both sides of an interface while still undergoing a change in the index of refraction. Because of the interdependence of the spatial profile κ on n_{eff} for isotropic materials, Eqs. (2.2, 2.6), any change in one requires a change in the other. However, this work shows that with anisotropic materials, it is sufficient to keep the in-plane components of permittivity constant while the x-component is free to be changed, as long as the condition in Eq. (2.18) is satisfied. The anisotropic expression for n_{eff} was derived and it was shown that a change in ϵ^x enables a change in the index of refraction while ϵ^{yz} is still constant.

An approximate analytical approach to calculate the reflection and transmission coefficients for the anisotropic SPP supporting system was also derived in this chapter. It was shown that in the limit of weak scattering, this analytical approach matches that of the much more computationally intensive numerical results of COMSOL. A technique for approximating the inverse of a nearly diagonal matrix using a Taylor Series expansion was outlined and used in the derivation.

An application that will benefit from the scattering free 2D optics is that of electro-optics. It is possible to fabricate materials such that the permittivity can be altered by an applied electric field. By adjusting where the field is applied, it will be possible to manufacture optical elements such as lenses, prisms, and reflectors. The advantage to creating these elements by the use of electro-optics is that the elements can be *dynamically* created, destroyed, or otherwise altered. This will allow for an extremely fine-grained degree of control over surface waves.

The theory of utilizing anisotropic metamaterials to match the spatial profile of TM waves can be applied to other waveguide structures besides the surface wave presented for the bulk of this chapter. Anisotropic planar waveguides can also be designed to exhibit efficient light management.

In the third chapter, an approach to creating the anisotropic metamaterial that could be used in the second chapter was discussed. To fully explore the properties of the nanolayered strucutre, three methods for calculating permittivities and electromagnetic fields were shown. The Effective Medium Theory was derived for this example, and shown to be deficient for accounting for large variations in field due to large differences in constituent permittivities. For comparison purposes, the Transfer Matrix Method was also derived. In principle the Transfer Matrix Method is exact, but computationally expensive to use for a large number of layers. To overcome this problem, a Non-local effective medium theory was derived by assuming the layered structure is similar to a photonic crystal. It was shown that although still not as accurate as the transfer matrix, the extended effective medium theory greatly outperforms that of the conventional effective medium theory, while having comparable computation times. It was shown that the non-local EMT can accurately describe a real-world experimental version of the nano-layered system made of a gold-silica composite.

It was also shown that the layered system can support high-index modes that are confined to spatial areas as small as $\lambda/8$ This confinement can be used in applications such as nano-guiding of light like photonic funnels [45]. Being able to confine light to such a scale is important for waveguide-optical fiber coupling.

The fourth chapter describes another anisotropic metamaterial based on plasmonic wires in a dielectric host. It was shown that conventional Maxwell-Garnett theory could only be applied in the case of isotropically distributed wires and wire shapes. We derived that alteration of these properties, even with the same relative concentration, can have a profound effect on the calculated effective permittivities. We showed the analytical expressions to calculate these effective parameters, and showed via numerical simulations their accuracy.

5.1 Outlook

Future avenues of research in the above areas include taking a much deeper look at the role the metal incident modes play in the analytical approximation developed in Ch 2. Previous work in this area assumed that these were negligable and played no role in the ensuing physics. We showed that they are indeed required, but the full understanding of their interaction with the SPP

is incomplete.

A possible application that is being explored is that of a lens based on the anisotropic metamaterial used as a substrate for a diffraction grating that allows for the imaging of a plane wave focussed as a point. The approach of calculating the scattering outlined in Ch. 2. is the basis for this future study.

We have shown multiple methods for constructing the anisotropic material. Experiments utilizing the anisotropic metamaterials for the non-magnetic left-handed system described in the introduction have been demonstrated with both the wire and layered systems. However, an experimental realization of the scattering-free plasmonic structure is yet to be completed.

The anisotropic metamaterials have also proven to be effective tools for subwavelength imaging and as a platform for extremely sensitive sensing. Further development of properties of the metamaterials will produce novel approaches to these areas of study.

An area of physics yet to be examined of the anisotropic metamaterials is their non-linear properties.

Many other future applications will benefit from the research in anisotropic metamaterials that was presented in this work as the approach is disseminated by other groups looking for solutions to unique problems.

BIBLIOGRAPHY

1. V. G. Veselago. The electrodynamics of substances with simultaneously negative values of and . *Physics-Uspekhi*, 10(4):509, 1968.

2. J. B. Pendry. Negative refraction makes a perfect lens. *Phys. Rev. Lett.*, 85(18):3966–3969, Oct 2000.

3. John B. Pendry and David R. Smith. Reversing light with negative refraction. *Physics Today*, 57(6):37–43, 2004.

4. Dror Sarid. Long-range surface-plasma waves on very thin metal films. *Phys. Rev. Lett.*, 47(26):1927–1930, Dec 1981.

5. Viktor A. Podolskiy and Evgenii E. Narimanov. Near-sighted superlens. *Opt. Lett.*, 30(1):75–77, 2005.

6. Zubin Jacob, Leonid V. Alekseyev, and Evgenii Narimanov. Optical hyperlens: Far-field imaging beyond the diffraction limit. *Opt. Express*, 14(18):8247–8256, 2006.

7. Jason Valentine, Shuang Zhang, Thomas Zentgraf, Erick Ulin-Avila, Dentcho A Genov, Guy Bartal, and Xiang Zhang. Three dimensional optical metamaterial exhibiting negative refractive index. *Nature*.

8. G. Alagappan, X. W. Sun, P. Shum, M. B. Yu, and M. T. Doan. One-dimensional anisotropic photonic crystal with a tunable bandgap. *J. Opt. Soc. Am. B*, 23(1):159–167, 2006.

9. Viktor A. Podolskiy and Alexander A. Govyadinov. Diffraction and dispersion management in active nanostructured metamaterials. volume 6638, page 66380Q. SPIE, 2007.

10. J. B. Pendry, D. Schurig, and D. R. Smith. Controlling Electromagnetic Fields. *Science*, 312(5781):1780–1782, 2006.

11. D. Schurig, J. J. Mock, B. J. Justice, S. A. Cummer, J. B. Pendry, A. F. Starr, and D. R. Smith. Metamaterial Electromagnetic Cloak at Microwave Frequencies. *Science*, 314(5801):977–980, 2006.

12. Otto L. Muskens, Silke L. Diedenhofen, Maarten H. M. van Weert, Magnus T. Borgstrom, Erik P.A.M. Bakkers, and Jaime Gomez Rivas. Epitaxial growth of aligned semiconductor nanowire metamaterials for photonic applications. *Advanced Functional Materials*, 18:1039–1046, 2008.

13. P.R. Evans, G.A. Wurtz, R. Atkinson, W. Hendren, D. O'Connor, W. Dickson, R.J. Pollard, and A.V. Zayats. Plasmonic core/shell nanorod arrays: Subattoliter controlled geometry and tunable optical properties. *Journal of Physical Chemistry C*, 111(34):12522–12527, 2007.

14. G. A. Niklasson, C. G. Granqvist, and O. Hunderi. Effective medium models for the optical properties of inhomogeneous materials. *Appl. Opt.*, 20(1):26–30, 1981.

15. K.K. Karkkainen, A.H. Sihvola, and K.I. Nikoskinen. Effective permittivity of mixtures: numerical validation by the fdtd method. *Geoscience and Remote Sensing, IEEE Transactions on*, 38(3):1303–1308, May 2000.

16. J.C. Maxwell Garnett. Colours in metal glasses and in metallic films. *Philosophical Transactions of the Royal Society of London, Series A, Containing Papers of a Mathematical or Physical Character*, 203:385–420, 1904.

17. J.C. Maxwell Garnett. Colours in metal glasses, in metallic films, and in metallic solutions–ii. *Philosophical Transactions of the Royal Society of London, Series A, Containing Papers of a Mathematical or Physical Character*, 205:237–288, 1906.

18. J.A. Stratton. *Electromagnetic Theory*. Read Books.

19. John David Jackson. *Classical Electrodynamics*. 1998.

20. J.B. Pendry, A.J. Holden, D.J. Robbins, and W.J. Stewart. Magnetism from conductors and enhanced nonlinear phenomena. *Microwave Theory and Techniques, IEEE Transactions on*, 47(11):2075–2084, Nov 1999.

21. Viktor A. Podolskiy and Evgenii E. Narimanov. Strongly anisotropic waveguide as a nonmagnetic left-handed system. *Physical Review B (Condensed Matter and Materials Physics)*, 71(20):201101, 2005.

22. H. Raether. *Surface Plasmons on Smooth and Rough Surfaces and on Gratings*. Springer-Verlag, Berlin, 1988.

23. Sergey I. Bozhevolnyi, Valentyn S. Volkov, and Kristjan Leosson. Localization and waveguiding of surface plasmon polaritons in random nanostructures. *Phys. Rev. Lett.*, 89(18):186801, Oct 2002.

24. S.A. Maier, P.G. Kik, H.A. Atwater, S. Meltzer, E. Harel, B.E. Koel, and A.A.G. Requicha. Local detection of electromagnetic energy transport below the diffraction limit in metal nanoparticle plasmon waveguides. *Nature Materials*, 2:229, 2003.

25. Igor I. Smolyaninov, Jill Elliott, Anatoly V. Zayats, and Christopher C. Davis. Far-field optical microscopy with a nanometer-scale resolution based on the in-plane image magnification by surface plasmon polaritons. *Physical Review Letters*, 94(5):057401, 2005.

26. Hocheol Shin and Shanhui Fan. All-angle negative refraction for surface plasmon waves using a metal-dielectric-metal structure. *Physical Review Letters*, 96(7):073907, 2006.

27. S.E. Bozhevolnyi, V.S. Volkov, E. Devaux, J.Y. Laluet, and T.W. Ebbesen. Channel plasmon subwavelength waveguide components including interferometers and ring resonators. *Nature*, 440:508, 2006.

28. W.L. Barnes, A. Dereux, and T.W. Ebbesen. Surface plasmon subwavelength optics. *Nature*, 424:824, 2003.

29. Mark I. Stockman. Nanofocusing of optical energy in tapered plasmonic waveguides. *Phys. Rev. Lett.*, 93(13):137404, Sep 2004.

30. R. Zia and M.L. Brongersma. Surface plasmon polariton analogue to young's double-slit experiment. *Nature Nanotechnology*, 2:426, 2007.

31. Zhaowei Liu, Jennifer M. Steele, Hyesog Lee, and Xiang Zhang. Tuning the focus of a plasmonic lens by the incident angle. *Applied Physics Letters*, 88(17):171108, 2006.

32. Igor I. Smolyaninov, David L. Mazzoni, Joseph Mait, and Christopher C. Davis. Experimental study of surface-plasmon scattering by individual surface defects. *Phys. Rev. B*, 56(3):1601–1611, Jul 1997.

33. M.I. D'yakonov. New type of electromagnetic wave propagating at an interface. *Sov. Phys. JETP*, 67(4):714–716, April 1988.

34. J.N. Gollub, D.R. Smith, D.C. Vier, T. Perram, and J.J. Mock. Experimental characterization of magnetic surface plasmons on metamaterials with negative permeability. *Phys. Rev. B*, 71:195402, 2005.

35. Justin Elser and Viktor A. Podolskiy. Scattering-free plasmonic optics with anisotropic metamaterials. *Physical Review Letters*, 100(6):066402, 2008.

36. Justin Elser, Viktor A. Podolskiy, Ildar Salakhutdinov, and Ivan Avrutsky. Nonlocal effects in effective-medium response of nanolayered metamaterials. *Applied Physics Letters*, 90(19):191109, 2007.

37. Robyn Wangberg, Justin Elser, Evgenii E. Narimanov, and Viktor A. Podolskiy. Nonmagnetic nanocomposites for optical and infrared negative-refractive-index media. *J. Opt. Soc. Am. B*, 23(3):498–505, 2006.

38. V.V. Schevchenko. *Continuous Transitions in Open Waveguides*. Golem, 1971.

39. R. F. Oulton, D. F. P. Pile, Y. Liu, and X. Zhang. Scattering of surface plasmon polaritons at abrupt surface interfaces: Implications for nanoscale cavities. *Physical Review B (Condensed Matter and Materials Physics)*, 76(3):035408, 2007.

40. P.J.B. Clarricoats and K.R. Slinn. Numerical method for the solution of waveguide-discontinuity problems. *Electronics Letters*, 2(6):226–228, June 1966.

41. Yi-Fan Chen, Peer Fischer, and Frank W. Wise. Negative refraction at optical frequencies in nonmagnetic two-component molecular media. *Physical Review Letters*, 95(6):067402, 2005.

42. Yi-Fan Chen, Peer Fischer, and Frank W. Wise. Chen, fischer, and wise reply:. *Physical Review Letters*, 98(5):059702, 2007.

43. COMSOL AB. Comsol multiphysics user's guide and rf module user's guide, 2008.

44. Justin Elser, Alexander A. Govyadinov, Ivan Avrutsky, Ildar Salakhutdinov, and Viktor A. Podolskiy. Plasmonic nanolayer composites: Coupled plasmon polaritons, effective-medium response, and subdiffraction light manipulation. *Journal of Nanomaterials*, 2007, 2007.

45. Alexander A. Govyadinov and Viktor A. Podolskiy. Metamaterial photonic funnels for subdiffraction light compression and propagation. *Physical Review B (Condensed Matter and Materials Physics)*, 73(15):155108, 2006.

46. Alexander A. Govyadinov and Viktor A. Podolskiy. Sub-diffraction light propagation in fibers with anisotropic dielectric cores. *J. of Modern Optics*, 53:2315–2324, 2006.

47. D. F. P. Pile and D. K. Gramotnev. Adiabatic and nonadiabatic nanofocusing of plasmons by tapered gap plasmon waveguides. *Applied Physics Letters*, 89(4):041111, 2006.

48. J. J. Burke, G. I. Stegeman, and T. Tamir. Surface-polariton-like waves guided by thin, lossy metal films. *Phys. Rev. B*, 33(8):5186–5201, Apr 1986.

49. Ivan Avrutsky. Guided modes in a uniaxial multilayer. *J. Opt. Soc. Am. A*, 20(3):548–556, 2003.

50. *Mathematica Documentation.*

51. W. T. Doyle and I. S. Jacobs. The influence of particle shape on dielectric enhancement in metal-insulator composites. *Journal of Applied Physics*, 71(8):3926–3936, 1992.

52. D. Schurig and D. R. Smith. Spatial filtering using media with indefinite permittivity and permeability tensors. *Applied Physics Letters*, 82(14):2215–2217, 2003.

53. Pavel A. Belov and Constantin R. Simovski. Subwavelength metallic waveguides loaded by uniaxial resonant scatterers. *Physical Review E (Statistical, Nonlinear, and Soft Matter Physics)*, 72(3):036618, 2005.

54. Gennady Shvets and Yaroslav A. Urzhumov. Engineering the electromagnetic properties of periodic nanostructures using electrostatic resonances. *Physical Review Letters*, 93(24):243902, 2004.

55. Dongmin Wu, Nicholas Fang, Cheng Sun, Xiang Zhang, Willie J. Padilla, Dimitri N. Basov, David R. Smith, and Sheldon Schultz. Terahertz plasmonic high pass filter. *Applied Physics Letters*, 83(1):201–203, 2003.

56. L.D. Landau, E.M. Lefshitz, and L.P. Pitaevskii. *Course of Theoretical Physics, 2nd Edition.* Reed, 1984.

57. Graeme W. Milton. *The Theory of Composites.* Cambridge University Press, 2002.

58. I.S. Gradshteyn and I.M. Ryzhik. *Table of Integrals, Series,and Products, Sixth Edition.* Academic Press, 2000.

59. Bruce T. Draine and Piotr J. Flatau. Discrete-dipole approximation for scattering calculations. *J. Opt. Soc. Am. A*, 11(4):1491, 1994.

60. Bruce T. Draine and Piotr J. Flatau. User guide for the discrete dipole approximation code ddscat 6.1, 2004.

61. A. L. Pokrovsky and A. L. Efros. Electrodynamics of metallic photonic crystals and the problem of left-handed materials. *Phys. Rev. Lett.*, 89(9):093901, Aug 2002.

62. Gennady Shvets, Andrey K. Sarychev, and Vladimir M. Shalaev. Electromagnetic properties of three-dimensional wire arrays: photons, plasmons, and equivalent circuits. 5218:156, 2003.

63. P. A. Belov, R. Marqués, S. I. Maslovski, I. S. Nefedov, M. Silveirinha, C. R. Simovski, and S. A. Tretyakov. Strong spatial dispersion in wire media in the very large wavelength limit. *Phys. Rev. B*, 67(11):113103, Mar 2003.

64. A. L. Pokrovsky and A. L. Efros. Nonlocal electrodynamics of two-dimensional wire mesh photonic crystals. *Phys. Rev. B*, 65(4):045110, Jan 2002.

APPENDICES

A APPENDIX Fortran Source Code for Nanowires

Fortran source code to calculate effective permittivity in the nanowired system (requires Intel compiler).

```
!  CDE_2D.f90
!
!  FUNCTIONS:
!  CDE_2D      - Entry point of console application.
!


!****************************************************************************
!
!  PROGRAM: CDE_2D
!
!  PURPOSE:  Entry point for the console application.
!
!****************************************************************************

    program CDE_2D

    include 'link_f90_static_smp.h'
    use ifcore

    implicit none

    ! Variables
    integer xMax
    integer nMax
    integer p !number of points that are inside the cylinder
    logical report
```

```
real*8 pi
real*8 r0, l0 ! radius of cylinder and distance between points, respectively
real*8 a0 ! parameter used in alp0 defintion
parameter (report=.false.)
parameter (xMax=10d0)
parameter (nMax=xMax**2d0, pi=3.141592653589793d0)
!parameter (a0=0.42d0)

!parameter (r0=0d0, p=1) ! Use a circle of radius 0
!parameter (r0=1d0, p=5) ! Use a circle of radius 1
!parameter (r0=2d0, p=13) ! Use a circle of radius 2
parameter (r0=3d0, p=29) ! Use a circle of radius 3
!parameter (r0=4d0, p=49) ! Use a circle of radius 4

real*8 xi(1:p*nMax) !x-coordinates of the particles
real*8 yi(1:p*nMax) !y-coordinates of the particles

real*8 xij(1:p*nMax, 1:p*nMax) !radii between the particles
real*8 yij(1:p*nMax, 1:p*nMax) !radii between the particles
real*8 rij(1:p*nMax, 1:p*nMax) !radii between the particles

! the following block may be marked as "complex*16"
real*8 alp0, chiX, chiY, chiXi, chiYi, eps
real*8 Gij(1:2*p*nMax, 1:2*p*nMax) ! Green function (the equation is d=E+G d)
real*8 Ei(1:2*p*nMax)
real*8 di(1:2*p*nMax)
real*8 c1, c2

integer iPiv(1:2*p*nMax)
```

```
      integer i,j,k, iter, nIter
      real*8 nIterTot
      real*8 r1, r2, dchi
      real*8 xx, yy, rr
      real*8 pSur,pMin,pMax,dP

      character*128 str

      ! Body of CDE_2D
      nIter=1 !number of iterations between the convergence check

      print*, 'Enter output file name'
      read(*,*) str
!     print*, 'Enter pMin,pMax,dP'
!     read(*,*) pMin,pMax,dP
!     print*, 'Enter epsInc'
!     read(*,*) eps

      pMin=0.3
      pMax=0.3
      dP=0.1
      eps=-10.0d0
!     str='a.out'

      open(unit=20, file=str, status='unknown')
      !open(unit=50, file='coord.txt', status='unknown')
      !write(20,*) 'Epsilon=',eps
      !write(20,*) 'xMax=',xMax
      !write(20,*) 'Number of points in cylinder=',p
```

```
    !write(20,*),'Format: p, epsX, epsY'

!    r0=1d0/sqrt(pi)
!    print*, 'enter r0'
!    read *, r0
!    r0=1d0/r0 !4.31165d0
!    r0=1d0/0.68
!    r0=1d0/0.65

    do pSur=pMin,pMax,dP
    !do eps=-10.0d0,10.0d0,0.02d0
    !do a0=0.1,1.0,0.025
    a0=0.575842d0
    !pSur=0.2d0
    l0=r0*sqrt(pi/pSur)
    alp0=a0**2d0*(eps-1)/(eps+1)/2d0
    !call rnset(7371702)

    chiX=0d0
    chiY=0d0
    dchi=0d0
    nIterTot=0d0

!    do while (dchi.gt.1d-3.or.nIterTot.eq.0d0)

    chiXi=0d0
    chiYi=0d0
    do iter=1,nIter
    if(report) print*,'        iter=',iter
    Ei(:)=1d0
```

```
    call coordinates(xi,yi,r0,xmax,nmax,p,l0)
    !print*, nmax
    if(report) print*,'        Coordinates calculated...'

    !do i=1, nmax !test to see if coordinates are correct
    !print*,xi(i),yi(i)
    !end do

    do i=1, p*nMax
    Ei(2*i-1)=1d0
    Ei(2*i)=0d0
    end do

    ! calculate the "separation" arrays
    do i=1,(p*nMax)
    do j=1,(p*nMax)
    xij(i,j)=xi(j)-xi(i)
    yij(i,j)=yi(j)-yi(i)
    rij(i,j)=sqrt(xij(i,j)**2d0+yij(i,j)**2d0)
!    write(50,*)i,j,xij(i,j),yij(i,j)
    if (rij(i,j).eq.0d0.and.i.ne.j) then
    print*,'Error: two particles have identical coordinates'
    stop
    end if
    end do
    end do
!    xij(:,:)=xij(:,:)*a0
!    yij(:,:)=yij(:,:)*a0
!    rij(:,:)=rij(:,:)*a0
```

```
! compute G-matrix
Gij(:,:)=0d0
do i=1,(p*nMax)
do j=1,(p*nMax)
xx=xij(i,j)
yy=yij(i,j)
rr=rij(i,j)

if (i.ne.j) then
! Gxx
Gij(2*i-1,2*j-1)=2d0*(2d0*xx**2d0/rr**2d0-1d0)/rr**2d0
! Gyy
Gij(2*i,2*j)=2d0*(2d0*yy**2d0/rr**2d0-1d0)/rr**2d0
! Gxy, Gyx
Gij(2*i-1,2*j)=4d0*yy*xx/rr**4d0
Gij(2*i,2*j-1)=4d0*yy*xx/rr**4d0
end if
end do
end do

!Gij=Iij-alp0 Gij
Gij(:,:)=-alp0*Gij(:,:)
do i=1,2*p*nMax
Gij(i,i)=1d0+Gij(i,i)
end do
if(report) print*,'        Gij calculated...'

!solve the Gij di=Ei
call dgetrf(2*p*nMax,2*p*nMax,Gij,2*p*nMax,iPiv,i)
```

```
   if (i.ne.0) then
   print*, 'zgetrf failed'
   stop
   end if
   if(report) print*,'        LU decomposition done...'
   call dgetrs('N',2*p*nMax,1,Gij,2*p*nMax,iPiv,Ei,2*p*nMax,i)
   if (i.ne.0) then
   print*, 'zgetrs failed'
   stop
   end if
   if(report) print*,'        Equations solved done...'
   di(:)=alp0*Ei(:)

   ! find epsilons
   do i=1,p*nMax
   chiXi=chiXi+di(2*i-1)
   chiYi=chiYi+di(2*i)
   end do
   end do !iter
   c1=chiX*nIterTot+chiXi/(real(xMax,8)*l0)**2d0 !/real(nMax,8)/a0**2d0
   c2=chiY*nIterTot+chiYi/(real(xMax,8)*l0)**2d0 !/real(nMax,8)/a0**2d0
   nIterTot=nIterTot+real(nIter,8)
   c1=c1/nIterTot
   c2=c2/nIterTot
   dchi=max(abs((c1-chiX)/c1),abs((c2-chiY)/c2))
   print*,'nIterTot=',nIterTot,';   dChi=',dchi
   chiX=c1
   chiY=c2

!   end do !while
```

```
    r1=1d0+4d0*pi*chiX
    r2=1d0+4d0*pi*chiY
    print*,'Converged'
    print*,r1
    print*,r2
    write(20,*)pSur,r1,r2
!    write(20,*)a0,r1,r2
!     write(20,*)eps,r1,r2
!    write(20,*)eps,a0,r1
    end do !pSur or a0
!    end do  !eps
    close(20)

    end program CDE_2D

    subroutine coordinates(xi,yi,r0,xmax,nmax,p,l0)!,nmaxG)
    implicit none
    integer i, j, k, l, p, xmax, nmax! k is the number of points inside the circle
    real*8 r0,l0
    !parameter (d=1d0)


    real*8 ai (1:nmax) !x-coordinate of the initial grid
    real*8 bi (1:nmax) !y-coordinate
    real*8 ri (1:nmax) !distance from center

    real*8 xo (1:p) !x-coordinate that is inside the cylinder
    real*8 yo (1:p) !y-coordinate that is inside the cylinder

    real*8 xi (1:p*nmax) !x-coordinate that is to be passed back to main
```

```
real*8 yi (1:p*nmax) !y-coordinate that is to be passed back to main

integer xc,yc ! sample center point of system used to determine how many
! points to use
xc=xmax/2
yc=xmax/2

open(unit=30, file='coordtest.txt', status='unknown')

do i=1, nmax
ai(i)=Mod(i-1,xmax)
bi(i)=AInt(real((i-1)/xmax))
end do

k=0
do i=1, nmax
ri(i)=sqrt((ai(i)-xc)**2+(bi(i)-yc)**2)
if (ri(i).le.r0) then
        k=k+1
        xo(k)=ai(i)-xc
        yo(k)=bi(i)-yc
endif
end do

! These are all the points in the mesh
l=0
do i=1, nmax
do j=1, k
l=l+1
xi(l)=ai(i)*l0+xo(j)
```

```
yi(l)=bi(i)*l0+yo(j)
write(30,*)xi(l),yi(l)
end do
end do

close(unit=30)

end subroutine
```

B APPENDIX Comsol Source Code for Nanowires

Source code for COMSOL script

```
clear fem appl
fem.sdim={'x' 'y'};


dr=5;
dr2=0.5;
% rad=.01;
xMax=10;


nMax=xMax^2;
xi=zeros(1,nMax);
yi=zeros(1,nMax);


elemLst=cell(1,nMax+3);
indArr=zeros(1,nMax+3);
indArr2=zeros(1,nMax+1);


a0=0.9;
b0=1./a0;
ax=1.;
bx=1./ax;
dRad=0.05;
radIni=0.05;
%radIni=0.45;
radFin=0.4;


concIni=0.01;
concFin=0.4;
```

```
dConc=0.02;

sqrt(ax*bx*concFin/pi/a0/b0)/ax
sqrt(ax*bx*concFin/pi/a0/b0)/bx

%nPts=floor((radFin-radIni)/dRad)+1;
nPts=floor((concFin-concIni)/dConc)+1;

dxFld=zeros(1,nPts);
exFld=zeros(1,nPts);
dyFld=zeros(1,nPts);
eyFld=zeros(1,nPts);
concArr=zeros(1,nPts);
epsX=zeros(1,nPts);
epsY=zeros(1,nPts);

epsOut=2.0;
epsIn=-2.5;
rad=radIni-dRad;
conc=concIni-dConc;
for k=1:nPts
%    rad=rad+dRad;
    conc=conc+dConc;
    rad=sqrt(ax*bx*conc/pi/a0/b0);
    concArr(k)=pi*a0*b0*rad^2/(ax*bx);

    for m=1:nMax
        r1=0.;
        xi(m)=mod(m-1,xMax) + r1;
    %    call drnun(1,r1)
```

```
        yi(m)=floor((m - 1)/xMax) + r1;
    end
    xi(:)=xi(:)*ax;
    yi(:)=yi(:)*bx;

    r1=rect2(-dr, ax*(xMax-1)+dr, -dr, bx*(xMax-1)+dr);
    r2=rect2(-dr+dr2, ax*(xMax-1)+dr-dr2, -dr+dr2,bx*(xMax-1)+dr-dr2);
    r3=rect2(-0.5, ax*(xMax-1)+0.5, -0.5, bx*(xMax-1)+0.5);

%    r1=rect2(-dr*ax, ax*(xMax-1+dr), -dr*bx, bx*(xMax-1+dr));
%    r2=rect2(-ax*dr+dr2, ax*(xMax-1+dr)-dr2,-dr*bx+dr2,bx*(xMax-1+dr)-dr2);
%    r3=rect2(-0.5*ax, ax*(xMax-0.5), -0.5*bx, bx*(xMax-0.5));

    elemLst{1}=r1;
    elemLst{2}=r2;
    elemLst{3}=r3;

    for m=1:nMax
%        elemLst(i+3)=circ2(xi(i),yi(i), rad);
        elemLst{m+3}=ellip2(a0*rad, b0*rad,'pos',[xi(m),yi(m)]);
    end

    fem.geom=geomcomp(elemLst);
%    figure(1);clf
%    geomplot(fem, 'sublabels', 'on');
%    drawnow;

    appl.mode.class='EmElectrostatics';
    appl.mode.type='cartesian';
```

```
indArr(:)=3;
indArr(1)=1;
indArr(2)=2;
indArr(3)=2;

appl.equ.elconstrel={'P' 'epsr' 'epsr'};
%appl.equ.epstype={[] 'iso' 'aniso'};
appl.equ.epsilonr={[] epsOut epsIn};
%appl.equ.epsrtensor={[] [] {epsIn/2,epsIn}};
appl.equ.P={{'1' '1'} [] []};
appl.equ.ind=indArr;

appl.var.epsilon0=1;

fem.appl=appl;
fem=multiphysics(fem);

fem.mesh=meshinit(fem);
fem.xmesh=meshextend(fem);
fem.mesh=meshrefine(fem);
fem.xmesh=meshextend(fem);
fem.mesh=meshrefine(fem);
fem.xmesh=meshextend(fem);

fem.sol=femlin(fem);

%    figure(2);clf
%    postplot(fem,'tridata','Ex','tribar','on');
%    drawnow;
```

```
%    figure(3);clf
%    postplot(fem,'tridata','Dx','tribar','on');
%    drawnow;

    for m=1:nMax+1
        indArr2(m)=m+2;
    end
    dxFld(k)=postint(fem,'Dx','dl',indArr2);
    exFld(k)=postint(fem,'Ex','dl',indArr2);
    epsX(k)=dxFld(k)/exFld(k);

    dyFld(k)=postint(fem,'Dy','dl',indArr2);
    eyFld(k)=postint(fem,'Ey','dl',indArr2);
    epsY(k)=dyFld(k)/eyFld(k);
end

save epsX.dat concArr epsX -ASCII
save epsY.dat concArr epsY -ASCII
save fldx.dat concArr dxFld exFld -ASCII
save fldy.dat concArr dyFld eyFld -ASCII
```

INDEX